578010

Department of Aerospace Engineering
The Pennsylvania State University

**FINAL REPORT**

# "Numerical Simulations for Landing Gear Noise Generation and Radiation"

**NASA Grant 210NRA-98-LaRC-5**

NASA Langley Research Center

Submitted by Principal Investigators:

Philip J. Morris
Boeing/A.D. Welliver Professor of Aerospace Engineering

Lyle N. Long
Professor of Aerospace Engineering

April 2002

# CHAPTER 1: LANDING GEAR AERODYNAMIC NOISE PREDICTION USING UNSTRUCTURED GRIDS

Frederic J. Souliez*, Lyle N. Long†, Philip J. Morris‡ and Anupam Sharma*
Department of Aerospace Engineering
The Pennsylvania State University
University Park, PA 16802

## Abstract

Aerodynamic noise from a landing gear in a uniform flow is computed using the Ffowcs Williams-Hawkings (FW-H) equation. The time accurate flow data on the surface is obtained using a finite volume flow solver on an unstructured grid. The Ffowcs Williams-Hawkings equation is solved using surface integrals over the landing gear surface and over a permeable surface away from the landing gear. Two geometric configurations are tested in order to assess the impact of two lateral struts on the sound level and directivity in the far-field. Predictions from the Ffowcs Williams-Hawkings code are compared with direct calculations by the flow solver at several observer locations inside the computational domain. The permeable Ffowcs Williams-Hawkings surface predictions match those of the flow solver in the near-field. Far-field noise calculations coincide for both integration surfaces. The increase in drag observed between the two landing gear configurations is reflected in the sound pressure level and directivity mainly in the streamwise direction.

## Nomenclature

$c$ speed of sound

---

* Graduate Research Assistant, Student Member AIAA

† Professor, Associate Fellow AIAA

‡ Boeing / A.D. Welliver Professor, Fellow AIAA

| | |
|---|---|
| $D$ | Wheel diameter |
| $H(f)$ | Heaviside function, $H(f) = 0$ for $f < 0$ and $H(f) = 1$ for $f > 0$ |
| $L_i$ | refer equation 2 |
| $\mathbf{M}$ | local Mach number vector of the source |
| $M$ | $\lvert\mathbf{M}\rvert$ |
| $M_r$ | $M_i \hat{r}_i$ |
| $\hat{n}$ | unit normal vector to the surface |
| $P_{ij}$ | compressive stress tensor |
| $p$ | pressure |
| $p_\infty$ | freestream pressure |
| $p'$ | acoustic pressure ( $p - p_\infty$ ) |
| $p_{RMS}$ | root mean square pressure perturbation |
| $r$ | distance from source to observer |
| $\hat{r}$ | unit normal vector from source to observer |
| $ret$ | retarded (source) time |
| SPL | Sound Pressure Level (dB) |
| $T_{ij}$ | Lighthill stress tensor |
| $t$ | observer time |
| $U_\infty$ | freestream velocity |
| $U_i$ | refer equation 2 |
| $u_i$ | $i^{th}$ fluid velocity component |
| $v_i$ | $i^{th}$ surface velocity component of integration surface f = 0 |

$\mathbf{x}$ observer location vector

$\delta(f)$ Dirac delta function, unity for $f = 0$, zero otherwise

$\rho$ density

$\rho_0$ free-stream density

$\tau$ retarded time

$\Box^2$ wave operator $1/c^2\,\partial^2/\partial t^2 - \nabla^2$

## Introduction

The Ffowcs Williams-Hawkings (FW-H) equation has recently been used with permeable surfaces in order to predict aerodynamic noise[1,2]. It is an inexpensive method to include the quadrupole source terms inside the FW-H surface without performing any volume integrations. This can significantly improve the accuracy of the noise predictions at locations where nonlinear interactions in the flow cannot be ignored. This is notably the case with highly turbulent flows such as high Reynolds number jets and wakes. It is also only slightly more expensive to use than a moving Kirchhoff surface (see Özyörük and Long[3]), but without the limitations of Kirchhoff methods.

The motivation for predicting the far-field noise generated by a 4-wheel landing gear stems from the increasing contribution of airframe noise to the overall sound level of an aircraft in its landing approach. Early studies in the 1970's by Heller and Dobrzynski[4] showed that high-lift devices such as slats and flaps, as well as deployed gears, generated noise levels 10 dB higher than those of an aircraft in its "clean" cruise configuration. Aerospatiale (now EADS Airbus) investigated the noise produced by several Airbus airplanes, which seems to indicate that noise from high-lift devices is likely to dominate

for medium size aircraft, while landing gear noise seems more of a problem for existing and future high capacity aircraft. The importance of investigating landing gear noise is reinforced by Airbus Industry plans to extend the Airbus family towards a high capacity aircraft.

Heller and Dobrzynski carried out a series of tests with both scale models[4] and full scale models[5], which underscored the lack of detailed geometric features with model-scale experiments and their effects on high frequency noise. These early experiments also showed that there is an increase in noise radiation from tandem axle configurations, which is the second test case in the present study. However, it was also found during the full scale experiment that struts, braces and other small features contribute significantly to the overall sound level. A more recent work by Dobrzynski et al[6] where the impact of various gear sizes and configurations is measured, illustrates the difficulty in using scale-model results for full-scale noise predictions. The actual simulation of the landing gear flow field is also of interest since it potentially affects the inflow of flaps located downstream. This was experimentally shown by Stoker et al[7] during a wind tunnel investigation of the airframe noise radiated by a model-scale Boeing 777, in which case a second high-frequency noise source from the flap system is only seen in the presence of the landing gear. This landing gear – flap interaction noise source was even shown to increase significantly by using a highly detailed gear geometry.

As already performed in a previous study by the same authors[8], the goal here is to combine the flexibility of unstructured grids with the FW-H equation. We use the Parallel Unstructured Maritime Aerodynamics (PUMA) code for generating the flow data. PUMA has been validated in several instances for simulating time-accurate flow

data[9,10]. The aim in the present case is to evaluate the impact on the noise directivity and intensity of two landing gear geometries (LDG1 and LDG2). It is expected to observe larger pressure fluctuations and a more complex three-dimensional flow in the case involving two additional struts (LDG2).

## The Computational Grids

The grids used for the simulation of the flow over both landing gear configurations were generated using the commercial package Gridgen by Pointwise, Inc. Figure 1 and Figure 2 show an overall view of the meshes on the landing gear surfaces with and without lateral struts respectively. The first mesh consists of about 80,000 surface triangles, for a total of about 880,000 tetrahedra in the volume mesh. The second mesh reused as much of the previous grid features as possible. With two additional struts, the number of triangles on the surface went up to 135,000, with about 1.2 million tetrahedral cells. Specific attention was given to the cell clustering between the front and rear wheels, in order to capture as much of the wake from the upstream wheel impinging on the downstream wheel. Flow separation from the fore wheel and wake impingement on the aft are expected to generate large unsteady pressure fluctuations and therefore noise. With the second geometry, great care was given to the mesh refinement between the two lateral struts, with the aft strut in the wake of the fore strut. The smallest geometric features were not overly simplified, since they have been shown to generate high frequency noise as explained in a later section describing the Ffowcs Williams – Hawkings equation.

As shown in Figure 3 for the second geometry (LDG2), a porous FW-H integration surface was used in addition to the flow data collected on the landing gear surfaces themselves. This will help determine the magnitude of the quadrupole source term for this low Mach number flow. Permeable FW-H surfaces were used for both geometries, with about 13,000 triangles in the first case, and 15,500 triangles in the case including two lateral struts. This coarsening mesh away from the solid surface is due to computer limitations. It may not be able to support the higher frequency pressure fluctuations. The advantage of these porous surfaces is that they can capture quadrupole-like terms without having to perform any volume integration. FW-H surfaces can be used in regions dominated by nonlinear effects (unlike the Kirchhoff formulations).

The Gibbs-Poole-Stockmeyer algorithm[11] was used to speed-up the communication process between CPUs. As shown in Figure 4, this procedure divides the domain into slices that minimize the number of messages between each processor, so that each CPU exchanges data with at most two neighboring CPUs. The time step for the unsteady simulations is determined by the smallest cell characteristic length. At a CFL number of 0.95, this yields a time step of 0.86E-08 second for the first grid, and 1.90E-08 second for the second grid (due mostly to some improved CAD work in the original geometry file). The numerical conditions were dictated by the CFL3D run performed at Langley: the Reynolds number based on the wheel diameter is 1.25 million, for a free stream Mach number of 0.2. The actual wheel diameter of the landing gear model is 9.4 cm.

## Flow Solver

PUMA (Parallel Unstructured Maritime Aerodynamics) is the computer program that was used to run the unsteady calculations. It is a finite volume, Runge-Kutta time-marching code that solves the compressible Navier-Stokes equations and uses unstructured grids. It uses the Message Passing Interface (MPI) library for parallel implementation. Its scaling performance for the two configurations is illustrated in figure 5. The flop performance is slightly higher for the second case for any given number of CPUs, since the ratio of computation over communication is greater for a larger grid. The facility used to perform the computation is the latest our two Cost effective Computing Arrays (COCOA and COCOA2)[12]. COCOA2 is a Beowulf cluster comprised of 20 nodes each having dual 800 MHz Pentium III and 1 GB RAM. The cluster has dual fast-Ethernet on each node and all the nodes are connected using two HP2524 switches with channel bonding for increased data communication. These machines run Redhat Linux (version 7.0) and the gcc compiler.

For these simulations the inherent artificial dissipation provided by Roe's flux integration scheme acts as a sub-grid scale turbulence model. A parallel investigation on separated flow around a cone[13] shows that the implementation of a Large Eddy Simulation (LES) method using a Smagorinsky sub-grid scale model[14] may improve PUMA's accuracy to simulate both mean and turbulent quantities in the wake of a cone base flow. LES has already been used extensively to compute sound sources[15,16], but some recent work related to two-time statistics of LES data, would indicate that LES fields are too coherent if the eddy viscosity model does not include any random

backscatter[17]. One way to circumvent this may be the use of a dynamic LES, which is more likely to yield enough backscattering to decorrelate the fluid motion at large scales. An example of the use of a dynamic subgrid scale model combined with a Ffowcs Williams – Hawkings solver is given by Morris et al[18] in an attempt to simulate the jet noise for circular nozzles.

## Simulation Results

Simulations were carried out over two cycles based on the expected shedding frequency of the wheel diameter. Each simulation took about 90 days on 24 CPUs. It is worth mentioning that the existing amount of data for both gear configurations put a strain on the available capacity in terms of storage requirements: about 40 Gigabytes of data have been collected for the two calculations described in this study. Data were sampled only for the second cycle to minimize the effects of the starting conditions. Local time stepping was initially used to accelerate the convergence from free-stream conditions to a realistic state. This is achieved by assigning to each cell the maximum allowable time step for a given CFL number (pseudo time marching). Global time stepping is then turned on before unsteady data is sampled. In order to evaluate the total drag, the momentum deficit method is used by evaluating the velocity deficit in the wake of the landing gear. More details can be found in Rae and Pope[19]. Figure 6 shows the average velocity deficit right behind the second gear configuration. In the second gear case, there is a good qualitative agreement with experimental results published by Stoker[7] in the high-fidelity landing gear configuration. Figure 7 shows the drag forces computed by integrating the pressure on the gear surface (pressure drag) and using Pope's wake

deficit approach (labeled total drag). Results are shown for both gear configurations during approximately 7 milliseconds of simulated flow time, giving enough time for the fluid to cover three times the gear total length. The force coefficients (drag, lateral and vertical force) are the computed forces divided by the landing gear surface area and the dynamic pressure. The increase in overall drag due to the introduction of the lateral support struts is large since these components are not aerodynamically profiled and are comparable to flat plates facing the incoming fluid flow. Figure 8 illustrates the lateral forces stemming from the presence of these two struts.

One expects the far-field sound pressure level to reflect this unsteady loading in both its intensity and directivity. Figure 9, which is a display of the instantaneous distribution of pressure on the landing gear surface in its second configuration, shows the pressure on these support struts, as well as on the wheels. Figure 10 shows a 3D representation of some vortex filaments shedding off various gear components, and highlight the impact of the upstream elements' wake onto gear elements at downstream locations. The effect of these vortices is not completely captured by the FW-H surface which lies on the landing gear itself. However the permeable FW-H surface does account for all the effects induced by these filaments until they cross its boundaries.

## Far-Field Noise Prediction

Only recently has the FW-H equation been used on a permeable surface. di Francescantonio[20] was able to show that simply integrating the surface source terms on a porous FW-H surface does account for the quadrupole sources enclosed within the

surface. The FW-H equation is written in the standard differential form including all quadrupole, dipole and monopole source terms as

$$^{2}p'(\mathbf{x},t)=\frac{\partial^2}{\partial x_i \partial x_j}\left[T_{ij}H(f)\right]-\frac{\partial}{\partial x_i}\left[L_i\delta(f)\right]+\frac{\partial}{\partial t}\left[(\rho_0 U_n)\delta(f)\right] \tag{1}$$

Where $L_i$ and $U_n$ are defined as

$$U_n = U_i\,\hat{n}_i \qquad U_i=\left(1-\frac{\rho}{\rho_0}\right)v_i+\frac{\rho u_i}{\rho_0} \tag{2}$$

$$L_i = P_{ij}\,\hat{n}_j + \rho u_i\left(u_n - v_n\right)$$

The subscript n indicates the projection of a vector quantity in the surface normal direction. Using the solution to the above equation given in Brentner and Farassat[21] and neglecting the quadrupole terms, the pressure fluctuation at a given observer location **x** and time $t$ is (equation 3 below)

$$4\pi p'(\mathbf{x},t)=\int_{f=0}\left\{\left[\frac{\rho_0\dot{U}_n}{r\left(1-M_r\right)^2}\right]+\left[\frac{\rho_0 U_n c\left(M_r-M^2\right)}{r^2\left(1-M_r{}^3\right)}\right]\right\}_{ret} dS$$
$$+\int_{f=0}\left\{\frac{1}{c}\left[\frac{\dot{L}_r}{r\left(1-M_r\right)^2}\right]+\left[\frac{L_r-L_M}{r^2\left(1-M_r\right)^2}\right]+\left[\frac{L_r\left(M_r-M^2\right)}{r^2\left(1-M_r\right)^2}\right]\right\}_{ret} dS \tag{3}$$

**FW-H code validation**

In the absence (at the moment) of experimental acoustic data to compare to, an already-proven method was implemented: the use of the CFD results to validate the FW-H sound predictions. As was done by the authors in a previous test case[8], the pressure fluctuations computed by the flow solver PUMA at an observer in the near field were

compared with the predictions given by the FW-H post-processing utility. Although the near-field pressure fluctuations are large, and likely contain a great amount of hydrodynamic oscillations, the derivation of the FW-H equation is such that all pressure perturbations (acoustic and hydrodynamic) should be recovered. Examples in the near field are given by Farassat and Brentner[22] in the case of high-speed impulsive noise at rotor blade tip Mach number close to 0.9. It is assumed that at a Mach number of 0.2, the quadrupole terms do not contribute significantly to the far-field noise. The solution $p'_Q$ to the quadrupole term of the FW-H equation is:

$$4\pi\, p'_Q(\mathbf{x},t) = \frac{\partial^2}{\partial x_i \partial x_j} \int_{-\infty}^{t} \int_{f>0} \frac{T_{ij}}{r}\, c\, d\Omega\, d\tau \tag{4}$$

The volume integration, if performed, must be carried out over a large volume and represents a large computational task. The far field approximation of equation 4 reduces to:

$$4\pi\, p'_Q(\mathbf{x},t) = \frac{1}{c}\frac{\partial^2}{\partial t^2} \int_{-\infty}^{t} \int_{f>0} \frac{T_{rr}}{r}\, d\Omega\, d\tau \tag{5}$$

However, there is in the present case an interest in capturing quadrupole effects in the near field, so that an exact result to the FW-H is needed instead of the far field approximation. Farassat and Brentner[23] decomposed the quadrupole noise term into three components varying with 1/r, $1/r^2$ and $1/r^3$ respectively:

$$4\pi\, p'_Q(\mathbf{x},t) = \frac{1}{c}\frac{\partial^2}{\partial t^2}\int_{-\infty}^{t}\int_{f>0}\frac{T_{rr}}{r}\,d\Omega\,d\tau \tag{6}$$

$$+\ \frac{\partial}{\partial t}\int_{-\infty}^{t}\int_{f>0}\frac{3T_{rr}-T_{ii}}{r^2}\,d\Omega\,d\tau$$

$$+\ c\int_{-\infty}^{t}\int_{f>0}\frac{3T_{rr}-T_{ii}}{r^3}\,d\Omega\,d\tau$$

There is a possibility that the second and third terms may contribute in a significant way to the near field pressure variations. This implies that in order to validate the FW-H predictions against the CFD results one may have to account for some of these nonlinear effects in addition to loading noise in the near field since the observer is in a highly perturbed propagating medium. In the current derivation of the FW-H equation, the quadrupole term is not computed (to reduce computing time and to limit storage requirements). However the porous FW-H surface shown in a previous figure has the ability to recover all nonlinear effects occurring within its own boundaries. Figure 11 is an illustration of the instantaneous pressure distribution on the permeable FW-H integration surface.

Observers were placed just above the landing gear main leg (x = 2.68 cm, y = 0 cm and z = 17 cm for observer whose pressure is depicted in Figure 12), where the porous FW-H mesh is more refined, so that the FW-H predictions can take place using both the solid and the porous FW-H surfaces. An example of comparisons with the PUMA results at one of these near-field observer locations is shown in Figure 12. This shows good agreement between the porous FW-H surface predictions and the solver computation, whereas the solid FW-H surface misses by more than 50% some of the

pressure fluctuations. This demonstrates the ability of the second FW-H surface to predict the entire pressure oscillations, either of acoustic or hydrodynamic nature. It tends to suggest that quadrupole effects may represent a significant contribution to the overall near-field sound level even at moderate Mach numbers. Unless a volume integration is performed over the entire CFD domain, the entire pressure perturbation cannot be exactly reproduced where nonlinear effects are important and where vortices flow across the permeable FW-H surface.

As expected, the agreement between the predictions from the two FW-H surfaces improves in the far-field. Figure 13 shows the pressure time history at 40 radii from the landing gear at a 50 degree angle with respect to the downstream axis. The field produced by the coarser FW-H surface off the landing gear does not reflect the same high-frequency fluctuations given by the predictions coming from data collected on the gear itself. In view of experimental results described earlier, it was decided to use the solid FW-H surface to investigate the far-field noise directivity, where high-frequency signals are thought to be significant. Figure 14 below illustrates the decrease of the RMS pressure signal as one moves away from the landing gear along the downstream axis. Calculations were made at 20 observers from 25 wheel diameters down to 50 wheel diameters in the wake of the landing gear. Both FW-H surface data were used and compared with a trend line assuming a signal decaying with 1/r. As observed previously, the agreement between the two surface predictions improves with increasing distance from the landing gear. As one moves further away from the landing gear, it is seen by the observer as an acoustic compact source, and the signal intensity should decrease with the inverse of the distance from the source.

**Sound directivity patterns**

The sound directivity in the medium- and far-field requires the use of a parallel version of the FW-H post-processing program[8,24]. For each radii away from the landing gear, 72 observer locations are defined, so that a resolution of 5 degree angle is obtained. A total of 648 observer points were defined, and are illustrated in Figure 15, which shows the relative scale with respect to the landing gear. For both gear configurations, all three orientation planes were studied and the results are reported in Figures 16a to 16f, Figures 17a to 17f and Figures 18a to 18f for the first and second gear configurations from a streamwise, spanwise and vertical perpective respectively. Polar directivity plots at radial locations of 10, 15 and 20 radii from the gear are plotted separately from the locations further away (30 to 50 radii from the gear) for scaling issues. Sound Pressure Level (SPL) contours with a reference pressure of $6x10^{-5}$ Pa are also presented for radial locations varying from 25 to 50 radii from the landing gear. The scale for equivalent configurations is unchanged in order to allow for qualitative comparisons with respect to both directivity and intensity of the sound pressure signal. In Figures 16 to 18, the landing gear is not to scale, and is meant to illustrate which orientation axis is shown.

The drag augmentation is reflected in the sound directivity patterns of both configurations. The intensity of the RMS pressure is greatly increased along the streamwise direction for the second gear case (LDG2). This is due to the two support struts on the aerodynamic profile of the landing gear. Regarding the lateral noise, the two struts seem to interfere with the build-up of sound, so that the signal in the spanwise direction is less than that in the clean configuration, where varying lateral forces on the

gear leg create pressure levels in the far-field comparable to those along the streamwise direction. In both cases, the near-field pressure perturbations are dominated by the fluctuations in drag. Little noise is generated in the vertical direction since most of the lift and drag variations are generated on the main gear leg. The overall pressure field looks much more disturbed in the second gear configuration, illustrating the complex three-dimensionality of the noise-generating flow pattern.

## Conclusion

The flow field around two landing gear configurations of increasing complexity has been assessed. The wake deficit observed behind the landing gear is very similar to that experimentally measured on comparable configurations. A parallel version of the Ffowcs Williams – Hawkings equation has been implemented using inexpensive Beowulf clusters to extract near- and far-field sound information. Both solid and permeable FW-H integration surfaces have been used. Excellent agreement has been obtained in the near field between the porous FW-H surface predictions and the CFD solver results where hydrodynamic fluctuations are expected to dominate and are of greater magnitudes than those typical of acoustic signals. More work is needed in order to show that the discrepancy observed between the solid and porous FW-H surfaces in the near-field is linked to short-range quadrupole-like effects even though the problem that was dealt with in the present case is a relatively low Mach number flow for this kind of effects to be significant.

The comparison of acoustic predictions produced by the two FW-H surfaces improves as the observer location is moved further away in the far field. The increase in

drag stemming from the lateral struts is reflected in the noise level and directivity. There is a significant increase in sound intensity in the streamwise direction, whereas the disturbance caused by these gear elements seems to interfere with the vortex shedding off the gear leg and the resulting lateral sound radiation.

## References


[1] Singer, B. A., Brentner, K. S., Lockard, D. P. and Lilley, G. M., "Simulation of Acoustic Scattering from a Trailing Edge", AIAA Paper 1999-0231, 37th Aerospace Sciences Meeting and Exhibit", Reno, NV, 1999.

[2] Singer, B. A., Lockard, D. P., Brentner, K. S., Khorrami, M. R., Berkman, M. E. and Choudhari, M., "Computational Aeroacoustic Analysis of Slat Trailing-Edge Flow", AIAA Paper 1999-1802, 5th AIAA/CEAS Aeroacoustics Conference, Greater Seattle, WA, 1999.

[3] Özyörük, Y. and Long, L. N., "A New Efficient Algorithm for Computational Aeroacoustics on Parallel Processors", Journal of Computational Physics, Vol. 125, pp. 135-149.

[4] Heller, H. H. and Dobrzynski, W. M., "Sound Radiation From Aircraft Wheel-Well/Landing-Gear Configurations", *J Aircraft*, vol. 14, no. 8, Aug. 1977, pp.768-774.

[5] Dobrzynski, W. M. and Buchholz, H., "Full-Scale Noise Testing on Airbus Landing Gears in the German Dutch Wind Tunnel", AIAA Paper 97-1597.

[6] Dobrzynski, W., Chow, L. C., Guion P. and Shiells, D., "A European Study On Landing Gear Airframe Noise Sources", AIAA Paper 2000-1971, 6th AIAA/CEAS Aeroacoustics Conference and Exhibit, Lahaina, HI, 2000.

[7] Stoker, R. W. and Sen, R., "An Experimental Investigation of Airframe Noise Using a Model-Scale Boing 777", AIAA Paper 2001-0987, 39th Aerospace Sciences Meeting and Exhibit", Reno, NV, 2001.

[8] Long, L. N., Souliez, F. and Sharma, A., "Aerodynamic Noise Prediction Using Parallel Methods on Unstructured Grids", AIAA Paper 2001-2196, 7th AIAA/CEAS Aeroacoustics Conference, Maastricht, The Netherlands, 2001.

[9] Modi, A. and Long, L. N., "Unsteady Separated Flow Simulations using a Cluster of Workstations", AIAA Paper 2000-0272, 38th Aerospace Sciences Meeting and Exhibit", Reno, NV, 2000.

[10] Sharma, A. and Long, L. N., "Airwake Simulations on LPD17 Ship", AIAA Paper 2001-2589, 31st AIAA Fluid Dynamics Conference and Exhibit, Anaheim, CA, 2001.

[11] Duff, I. S., Erisman, A. M. and Reid, J. K., Direct Methods for Sparse Matrices, Oxford University Press, 1986.

[12] Long, L. N. and Modi, A., "Turbulent Flow and Aeroacoustics Simulations using a Cluster of Workstations", Linux Revolution Conference, Champaign, IL, June 2001.

[13] Souliez, F. J., Parallel Methods for Computing Unsteady Separated Flows Around Complex Geometries, PhD thesis, Penn State University, 2002.

[14] Smagorinsky, J., "General Circulation Experiments with the primitive equations", Monthly Weather Review No. 91, pp. 99-165, 1963.

[15] Piomelli, U., "Large-Eddy Simulation: Achievements and Challenges", Progress in Aerospace Sciences 35 (1999), pp. 335-362.

[16] Seror, C., Sagaut, P., Bailly, C. and Juve, D., "On the Radiated Noise Computed by Large-Eddy Simulation", Phys. Fluids 13 (2001), pp. 476-487.

[17] He, G., Rubinstein, R. and Wang, L. P., "Effects of Eddy Viscosity on Time Correlations in Large Eddy Simulation", ICASE Report No. 2001-10.

[18] Morris, P. J., Scheidegger, T. E. and Long. L. N., "Jet Noise Simulations for Circular Nozzles", AIAA Paper 2000-2080, 6th AIAA/CEAS Aeroacoustics Conference and Exhibit, Lahaina, HI, 2000.

[19] Rae, W. H. and Pope, A., "Low-Speed Wind Tunnel Testing", second edition, Wiley-Interscience, 1984.

[20] di Francescantonio, P., "A New Boundary Integral Formulation for the Prediction of Sound Radiation", *Journal of Sound and Vibration* (1997) 202(4), pp. 491-509.

[21] Brentner, K. S., and Farassat, F., "An Analytical Comparison of the Acoustic Analogy and Kirchhoff Formulation for Moving Surfaces" *AIAA Journal*, Vol. 36, No .8, Aug. 1998, pp. 1379-1386.

[22] Farassat, F. and Brentner, K. S., "Supersonic Quadrupole Noise Theory for High-Speed Helicopter Rotors", *Journal of Sound and Vibration* (1998) 218(3), pp. 481-500.

[23] Farassat, F. and Brentner, K. S., "The Uses and Abuses of the Acoustic Analogy in Helicopter Rotor Noise Prediction", *Journal of the American Helicopter Society* (1988) 33, pp. 29-36.

[24] Long, L. N. and Brentner, K. S., "Self-Scheduling Parallel Methods for Multiple Serial Codes with Application to WOPWOP", Paper 2000-0346, 38th Aerospace Sciences Meeting and Exhibit", Reno, NV, 2000.

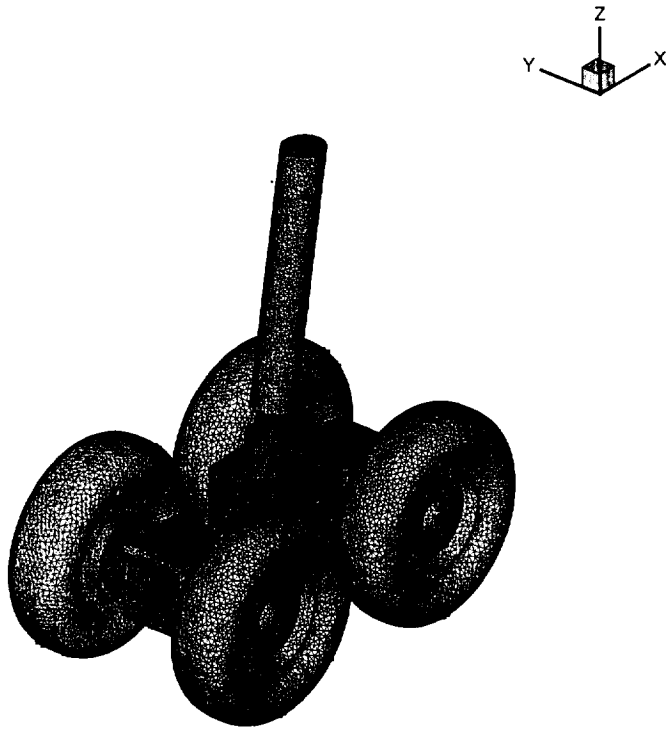


**Figure 1** Surface mesh of first landing gear configuration(LDG1)

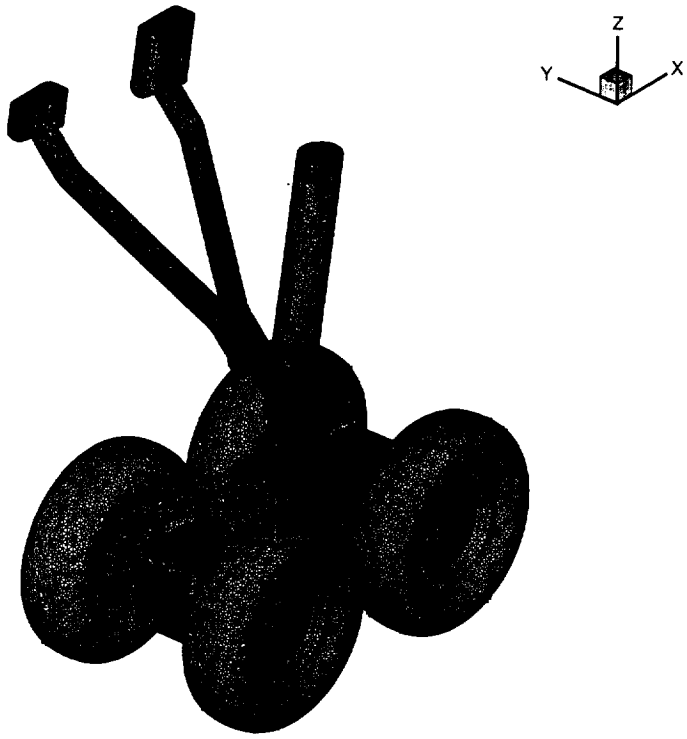


**Figure 2** Surface mesh of second landing gear configuration (LDG2)

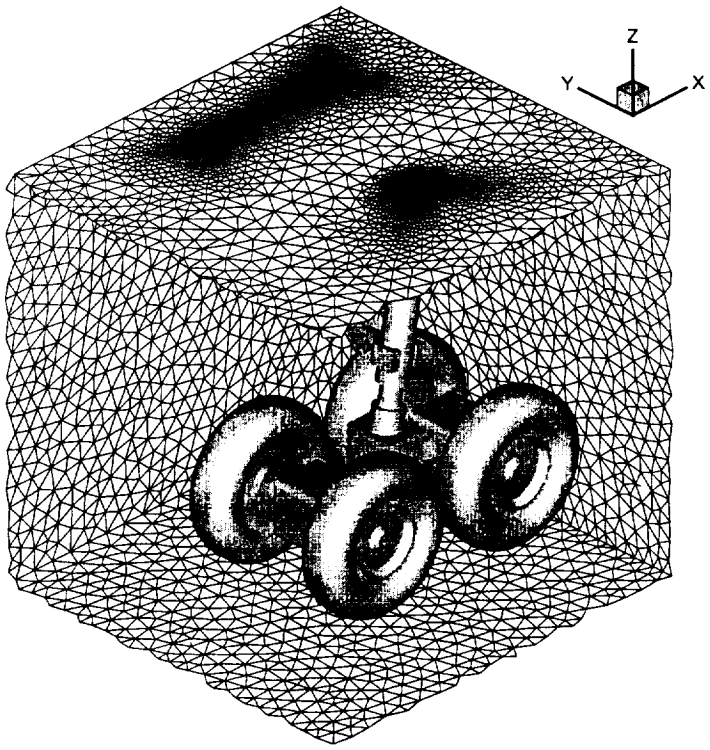


**Figure 3** Partial view of the porous FW-H surface around LDG2 gear configuration

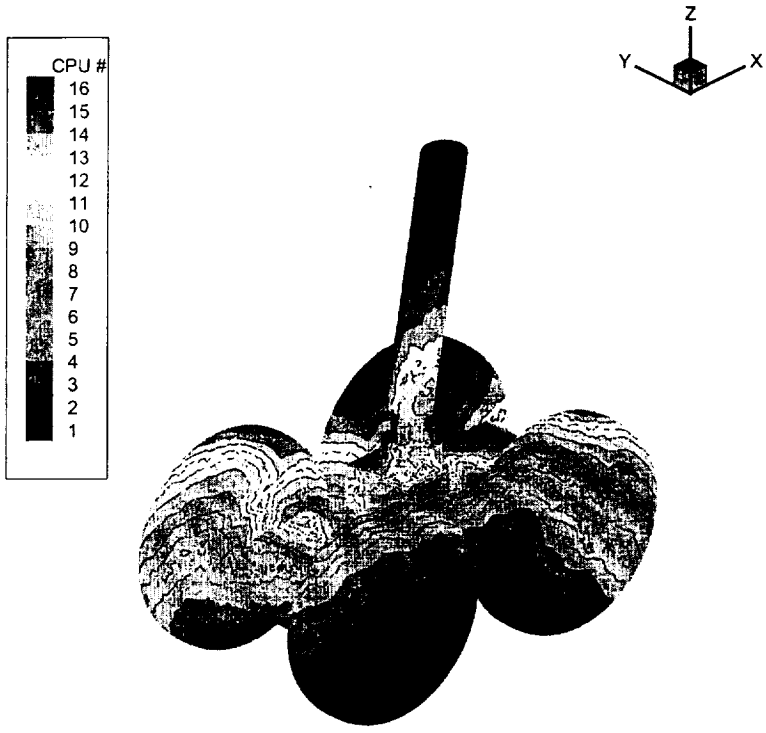


**Figure 4** GPS partitioning on LDG1 landing gear surface across 16 processors

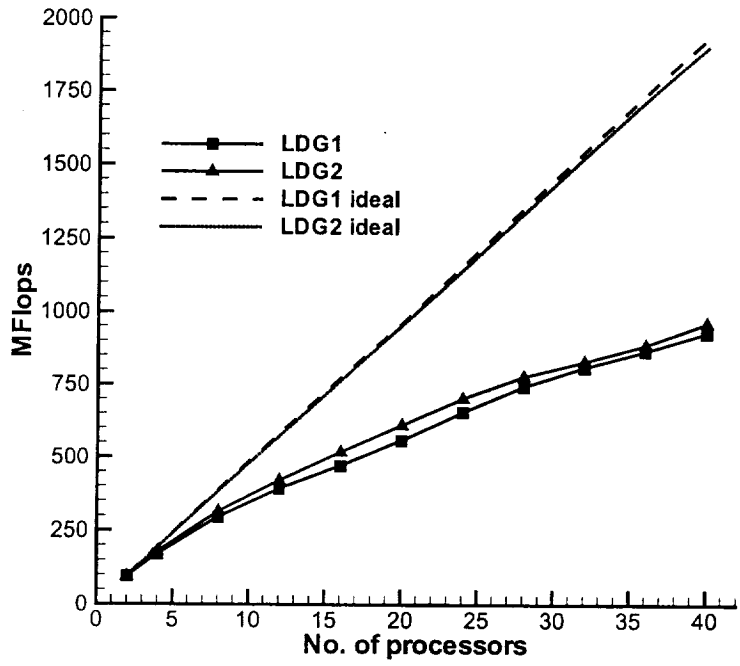


**Figure 5** Parallel speed up on COCOA2 for both landing gear configurations

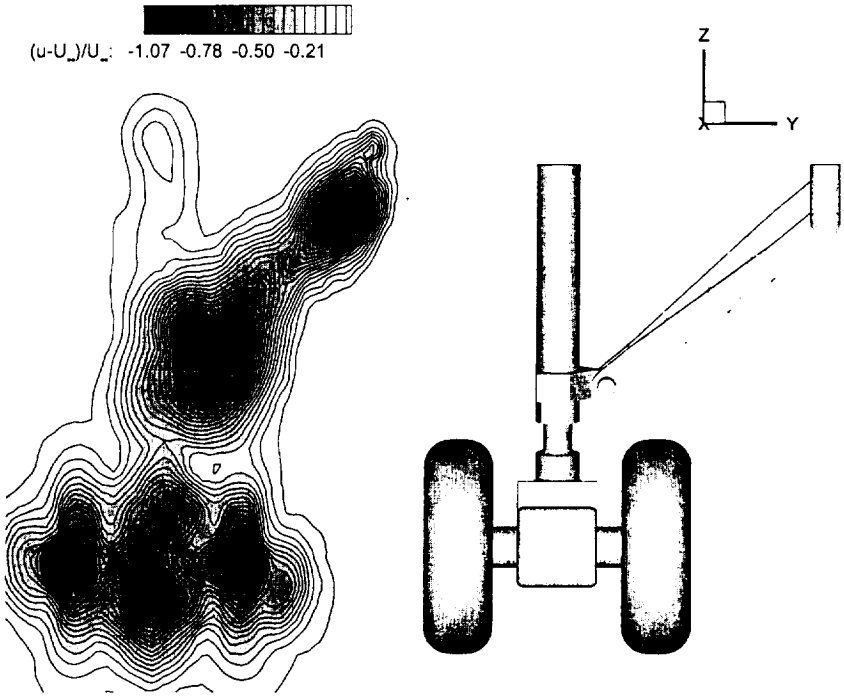


**Figure 6** Average velocity deficit in the wake of the LDG2 configuration

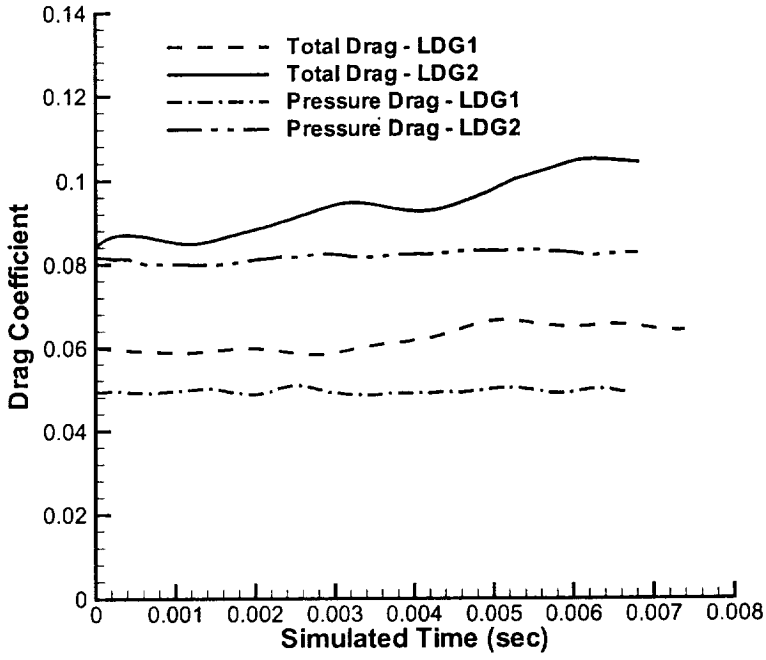


**Figure 7** Time-history of drag force coefficients for landing gear configurations LDG1 and LDG2 using pressure and wake methods

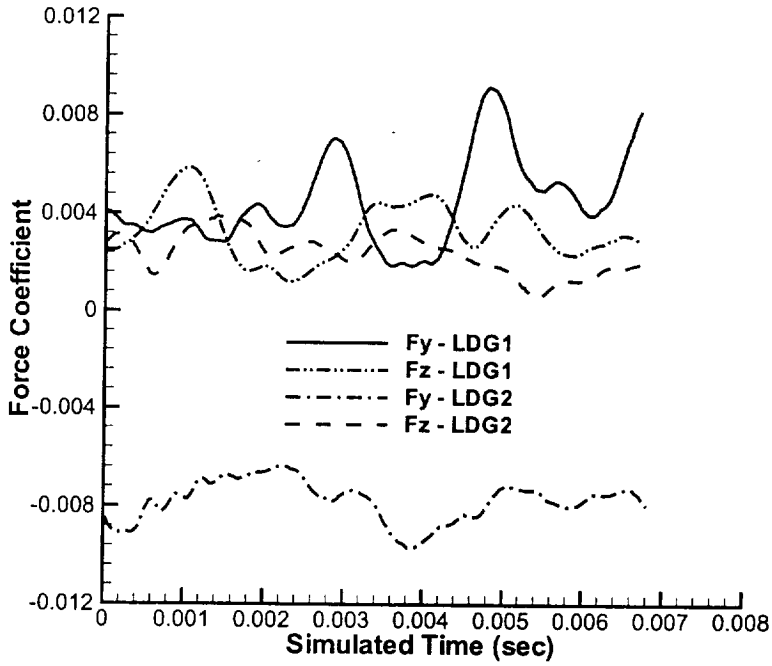


**Figure 8** Time-history of lateral (Fy) and vertical (Fz) pressure force coefficients for configurations LDG1 and LDG2

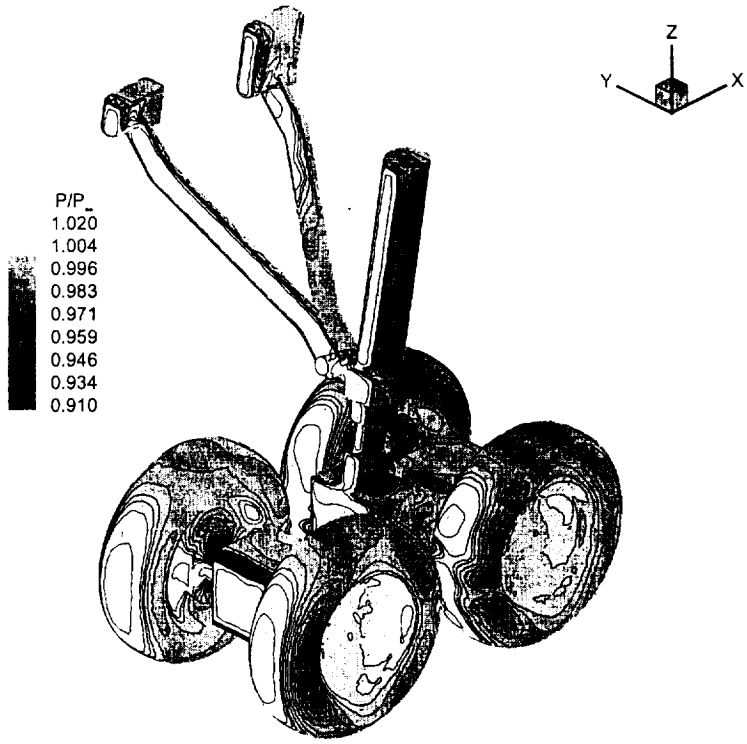


**Figure 9** Instantaneous pressure distribution for LDG2 configuration

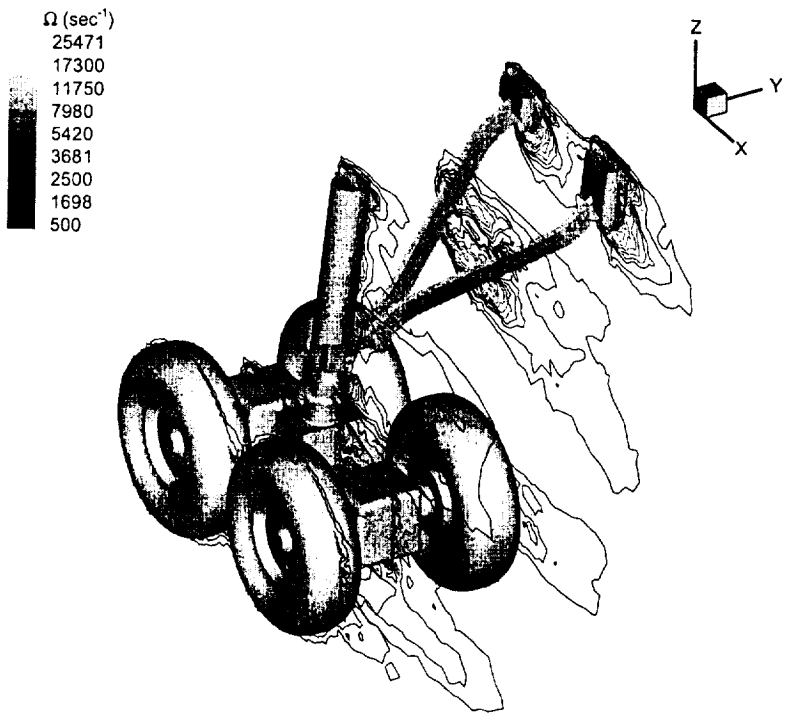


**Figure 10** Instantaneous vorticity filaments for the LDG2 configuration

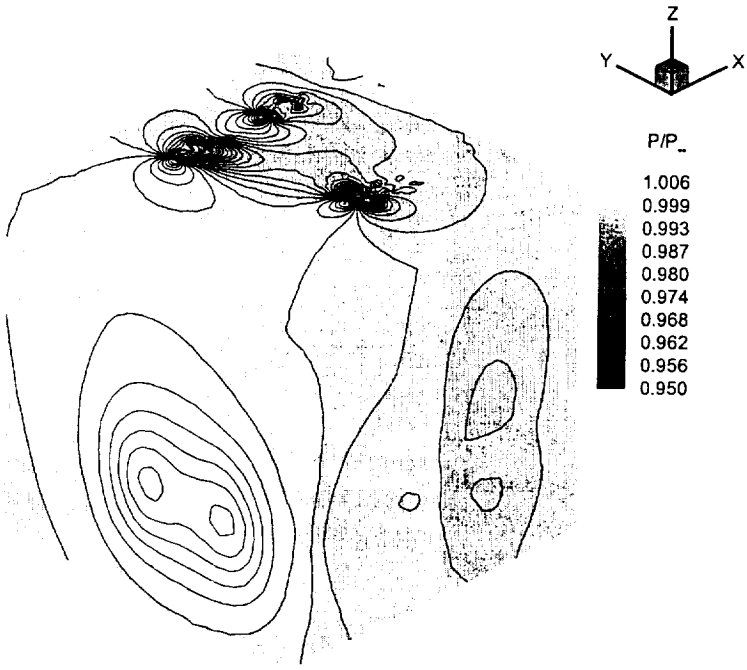


**Figure 11** Instantaneous pressure distribution on the permeable FW-H surface for the LDG2 configuration

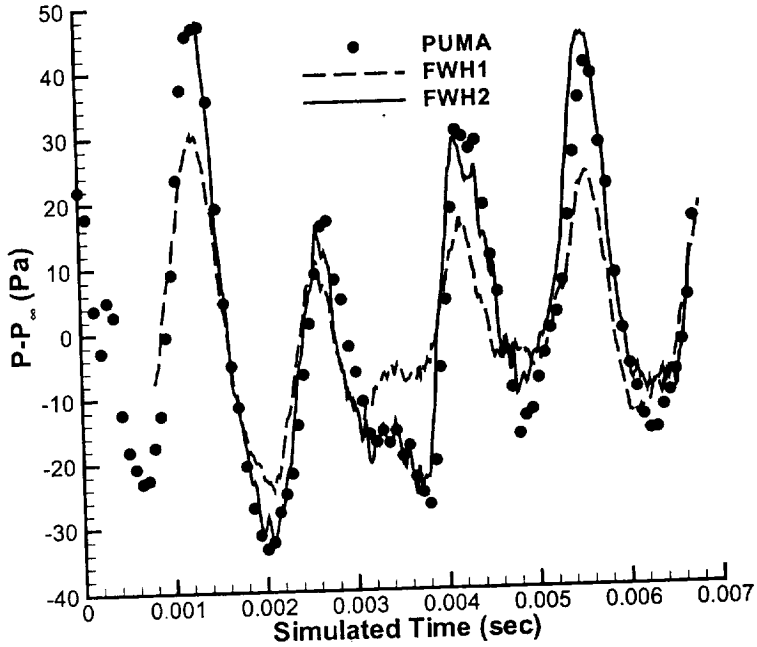


**Figure 12** Comparison in the near-field of the FW-H predictions from integration surfaces 1 and 2 versus the PUMA solver results

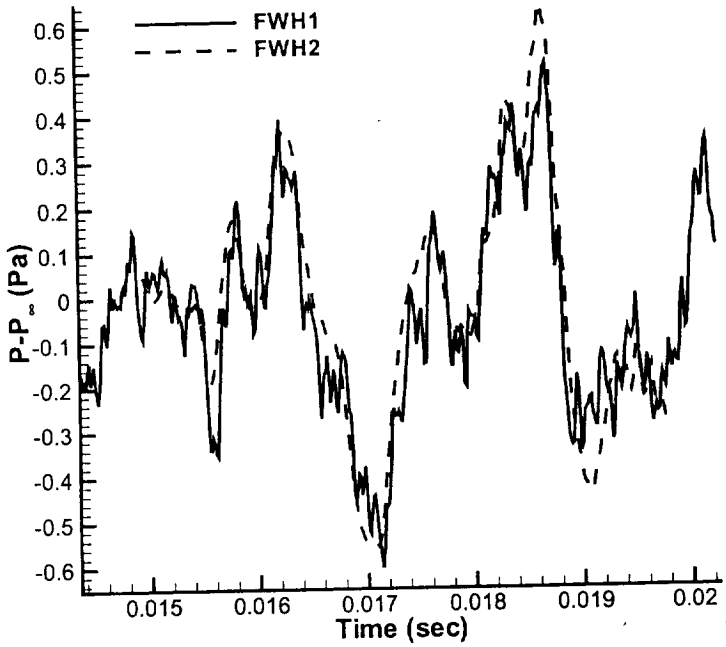


**Figure 13** Comparison of the FW-H predictions from integration surfaces 1 and 2 in the far-field

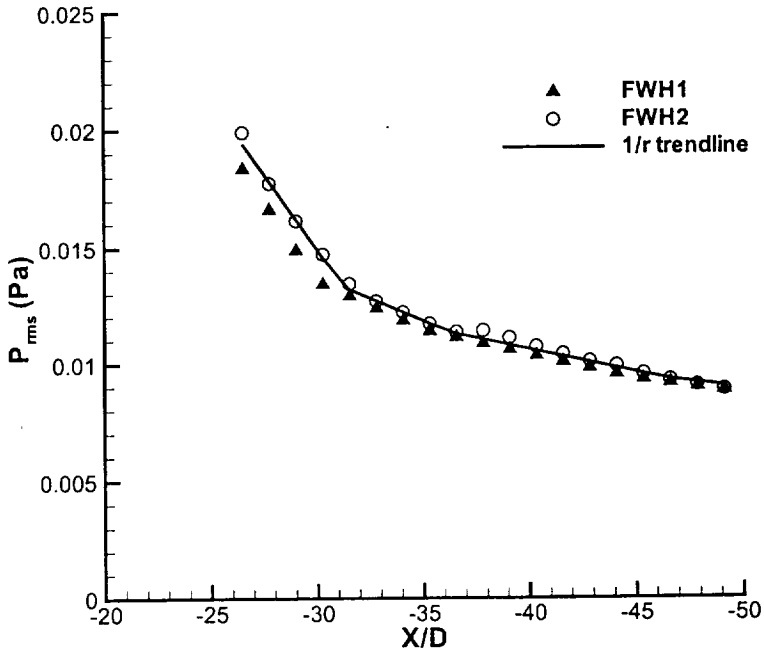


**Figure 14** RMS pressure signal predictions from integration surfaces 1 and 2 and trend lines

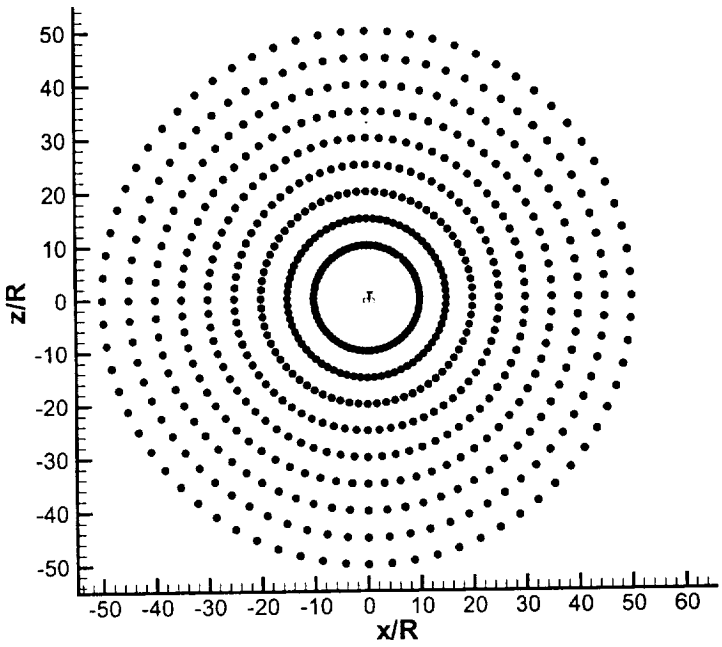


**Figure 15** Observer locations for sound directivity calculations

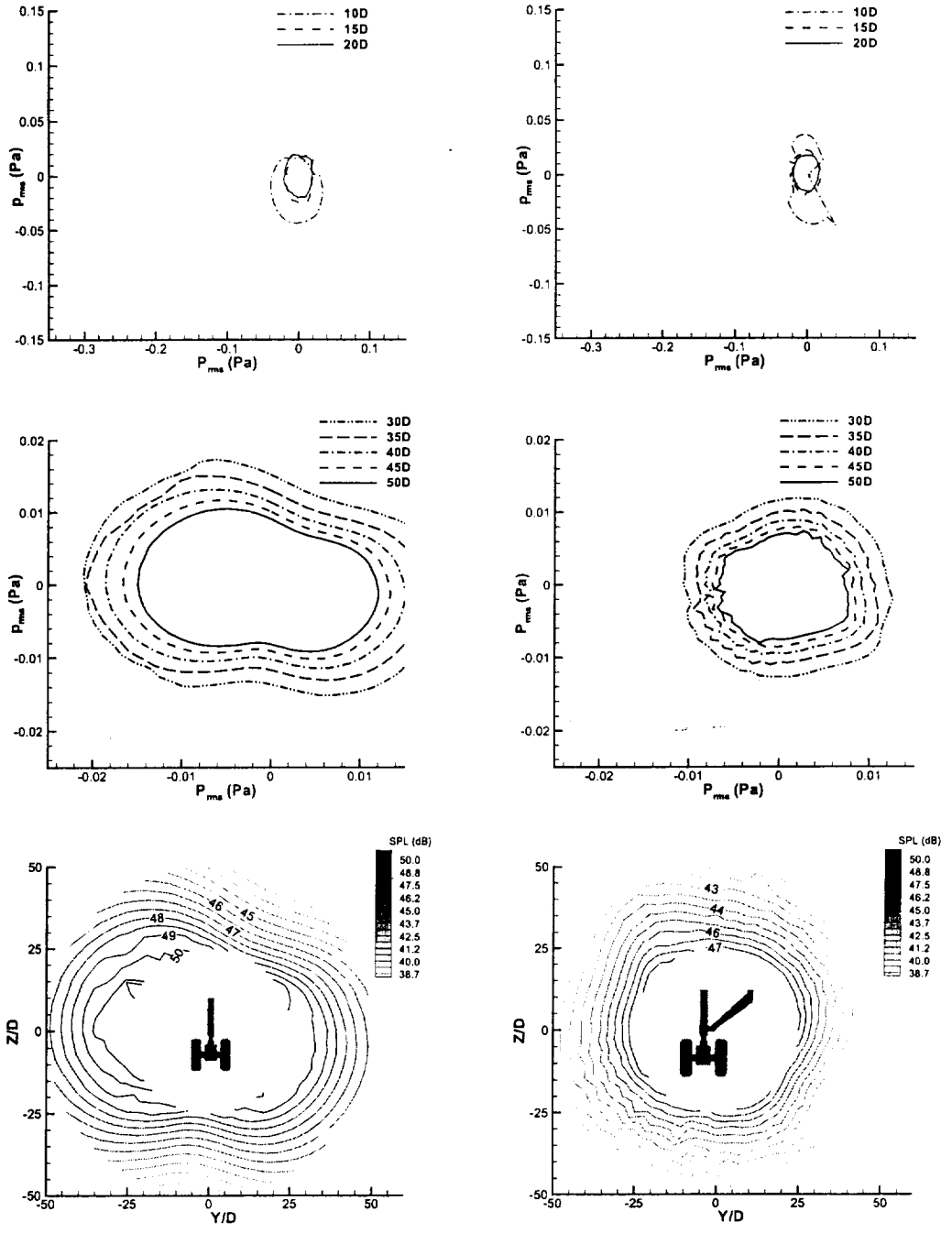


**Figure 16** (top) Medium-field RMS pressure, (middle) far-field RMS pressure and (bottom) SPL contour from streamwise perspective for LDG1 (left) and LDG2 (right)

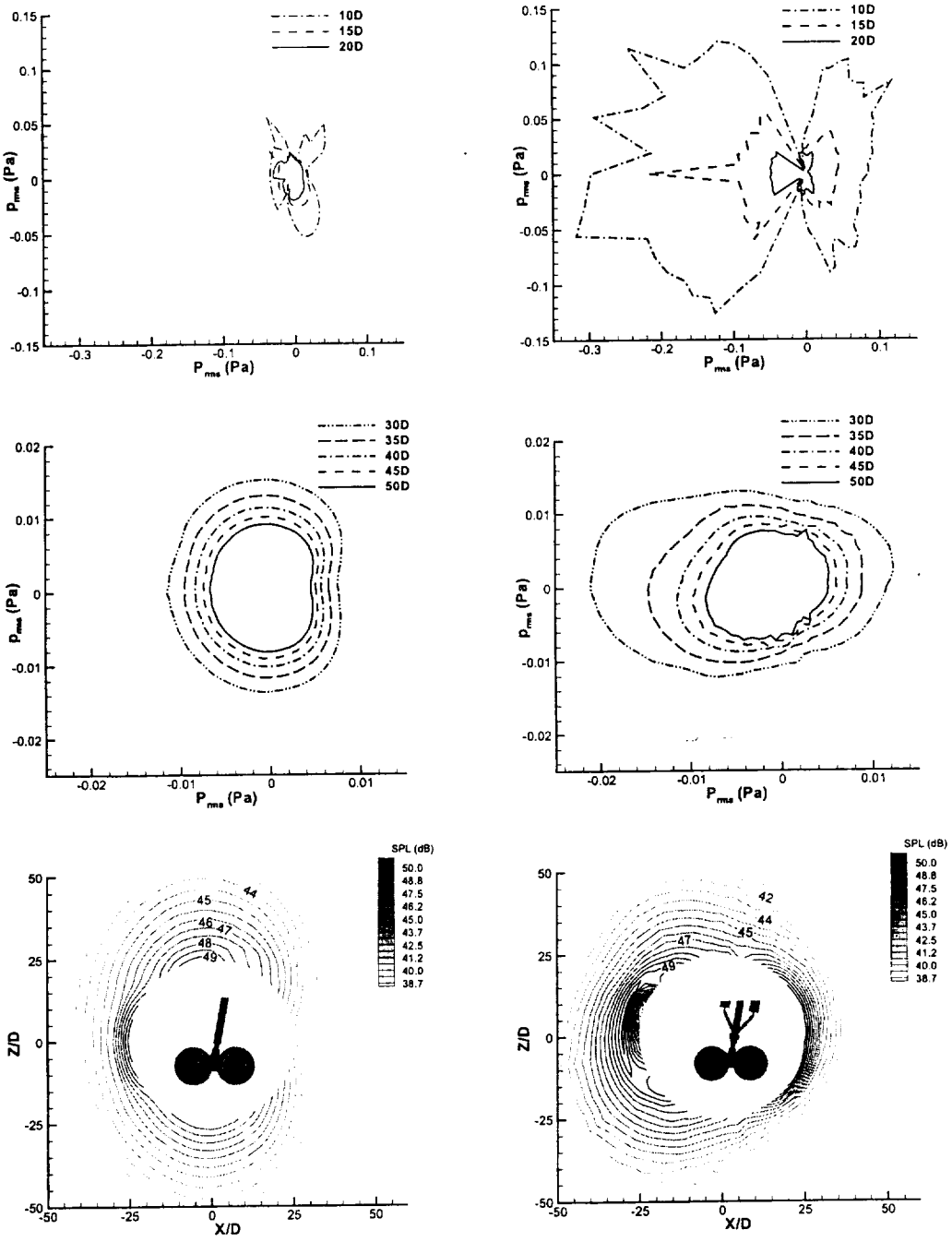


**Figure 17** (top) Medium-field RMS pressure, (middle) far-field RMS pressure and (bottom) SPL contour from sideways perspective for LDG1 (left) and LDG2 (right)

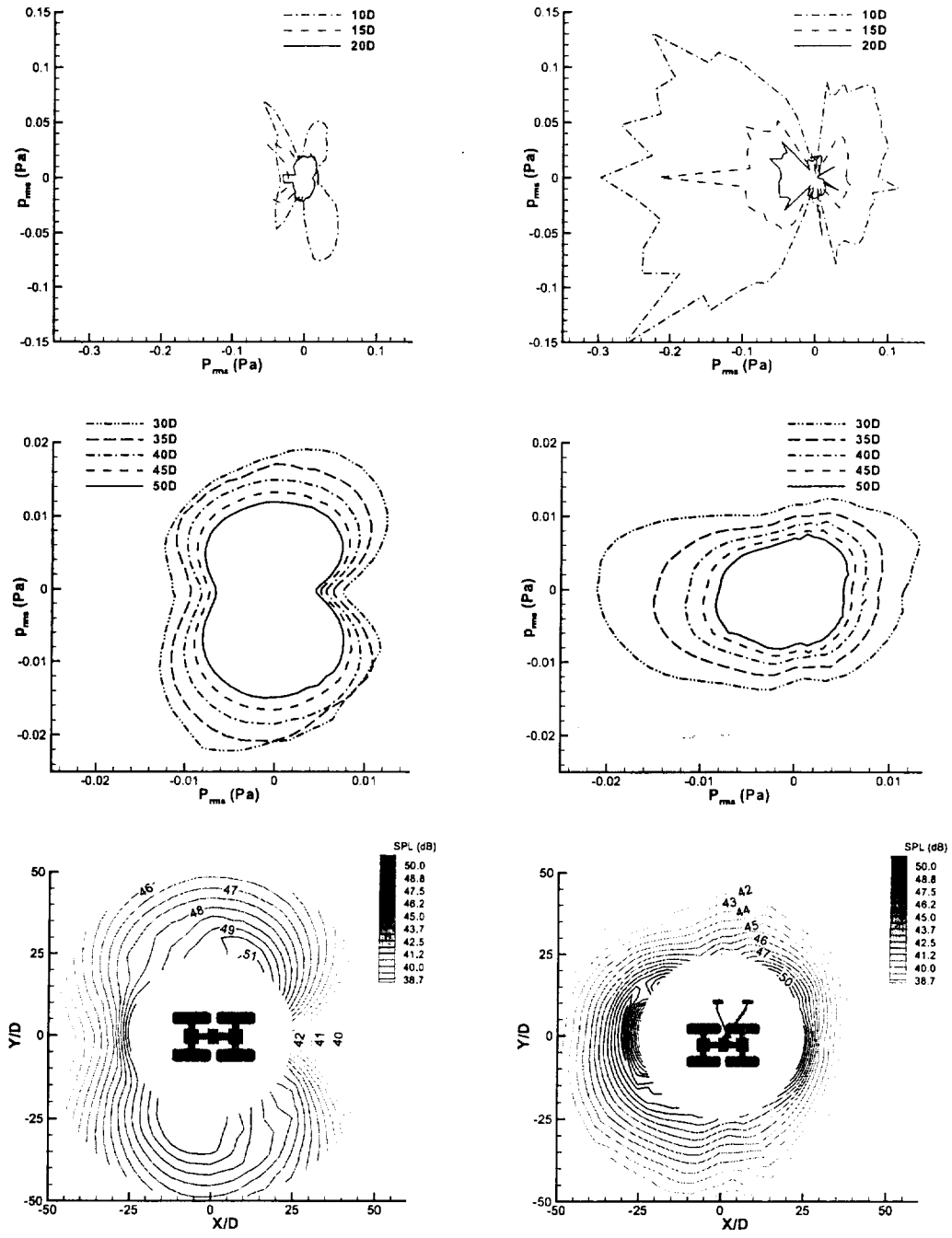


**Figure 18** (top) Medium-field RMS pressure, (middle) far-field RMS pressure and (bottom) SPL contour seen from above for LDG1 (left) and LDG2 (right)

# AERODYNAMIC NOISE PREDICTION USING PARALLEL METHODS ON UNSTRUCTURED GRIDS

Lyle N. Long*, Frederic Souliez† and Anupam Sharma†
*Department of Aerospace Engineering*
*The Pennsylvania State University, PA-16802*

**Aerodynamic noise from a cone in a uniform flow is computed using the Ffowcs Williams-Hawkings (FW-H) equation. The time accurate flow data is obtained using a finite volume flow solver on an unstructured grid. The FW-H equation is solved for surface integrals over a permeable surface away from the cone. Predictions from the FW-H code are compared with direct calculations by the flow solver at a few observer locations inside the computational domain. A very good qualitative match is obtained. Sound directivity patterns in the azimuthal and in the longitudinal directions are presented. The FW-H code is also validated against a model problem of a monopole in a uniform mean flow.**

## Nomenclature

| | |
|---|---|
| $C_p$ | coefficient of pressure |
| $C_s$ | sub-grid scale constant in Smagorinsky model |
| $c$ | sound speed in quiescent medium |
| $d$ | base diameter of the cone |
| $f_s$ | vortex shedding frequency (Hz) |
| $H(f)$ | Heaviside function, $H(f) = 0$ for $f < 0$ and $H(f) = 1$ for $f > 0$ |
| $L_i$ | refer Eq. 2 |
| $L_M$ | $L_i M_i$ |
| $L_r$ | $L_i \hat{r}_i$ |
| $\dot{L}_r$ | $\dot{L}_r \hat{r}_i$ |
| $\mathbf{M}$ | local Mach number vector of the source |
| $M$ | $\lvert\mathbf{M}\rvert$ |
| $M_n$ | $M_i \hat{n}_i$ |
| $M_0$ | $U_0/c$ |
| $M_r$ | $M_i \hat{r}_i$ |
| $\dot{M}_r$ | $\dot{M}_i \hat{r}_i$ |
| $\hat{\mathbf{n}}$ | unit normal vector to the surface, $n_i$ |
| $P_{ij}$ | compressive stress tensor with $p_o \delta_{ij}$ subtracted |
| $p$ | pressure |
| $p_0$ | freestream pressure |
| $p'$ | acoustic pressure, $p - p_o$ |
| $p'_{rms}$ | root mean squared pressure perturbation |
| $ret$ | retarted time |
| $T_{ij}$ | Lighthill stress tensor |
| $t$ | observer time |
| $\theta$ | angular location of the observer |
| $U$ | averaged streamwise velocity |
| $U_0, U_\infty$ | freestream velocity |
| $U_i$ | refer Eq. 2 |
| $U_n$ | $U_i \hat{n}_i$ |
| $\dot{U}_n$ | $\dot{U}_i \hat{n}_i$ |
| $U_{\dot{n}}$ | $U_i \dot{\hat{n}}_i$ |
| $u_i$ | components of local fluid velocity |
| $u'_{avg}$ | averaged streamwise perturbation velocity |
| $u_n$ | $u_i \hat{n}_i$ |
| $v_n$ | local normal velocity of the source surface |
| $\delta(f)$ | Dirac delta function $\delta(f) = 1$ for $f = 0$, otherwise $\delta(f) = 0$ |
| $\delta_{ij}$ | Kronecker delta function, $\delta_{ij} = 1$ for $i = j$, otherwise $\delta_{ij} = 0$ |
| $\rho$ | density of the fluid |
| $\rho_0$ | freestream density of the fluid |
| $\rho'$ | density perturbation, $\rho - \rho_o$ |
| $\Omega$ | vorticity ($s^{-1}$) |
| $\omega$ | angular frequency of the monopole source |
| $\Box^2$ | wave operator, $\Box^2 \sim (\frac{1}{c^2}\frac{\partial^2}{\partial t^2} - \nabla^2)$ |

## Introduction

RECENTLY, the Ffowcs Williams-Hawkings (FW-H) equation has been used with permeable surfaces for predicting aerodynamic noise. The application of FW-H in this manner effectively allows for the inclusion of the quadrupole source terms inside the surface without performing volume integrations. This has significantly improved the accuracy of noise prediction for cases where the contribution from nonlinear interactions in the flow cannot be ignored. This is typical of highly turbulent flows, for example, high Reynolds number jets and wakes.

The FW-H equation requires time accurate data on, and in the volume inside the permeable surface. This data is usually obtained by solving the Euler/Navier-Stokes equations accurately in time. Since the FW-H equation uses data from within the FW-H surface, the

*Professor, Assoc. Fellow, AIAA. lnl@psu.edu.
†Graduate Research Assistant, Pennsylvania State University

outer grid can be made coarse without much loss of accuracy. Unstructured grids provide great flexibility in distributing the grid in the domain, and hence can be used to cluster the cells inside the FW-H surface. This feature can be exploited to significantly increase the computation speed while keeping almost the same accuracy in predicting aerodynamic noise. This will also permit the modeling of complex geometries such as helicopter fuselages, landing gear, and flaps.

The goal here is to test the combination of unstructured grids with the FW-H equation in predicting the aerodynamic noise. The test case is chosen to be the flow over a cone. A cone has sharp edges which fixes the separation point. This makes the flow fairly Reynold's number independent.

We use the Parallel Unstructured Maritime Aerodynamics (PUMA)[1] code for generating the time-accurate flow data. PUMA has been validated for time-accurate computations.[2-4] The ultimate aim is to predict the airframe noise from complex geometries such as landing gear, slats, and flaps. This cone case may be considered as a benchmark problem.

## The Grid

The grid used for the simulation of the flow over a cone of vertex angle 60° was generated using Gridgen. Figure 1 shows an overall view of the mesh consisting of approximately 280,000 tetrahedra. The clustering was done around the cone and in the wake region with increasing cell size towards the outer boundaries of the computational domain. The reason for using Gridgen comes from one interesting feature of this commercial software: arbitrary surfaces can be created around the cone (one within the CFD domain boundaries and the other being the CFD domain boundary) and are sources for the meshing algorithm. It is possible to export separately any of these closed surfaces in a separate file, providing a means to extract flow data on the surface using a FW-H module that was added to the unstructured solver. The smallest cylinder was used as a porous FW-H surface. At the bounding faces of the CFD domain, Riemann boundary conditions were assigned at each face center, hence minimizing reflections from the boundaries into the computational domain. The large cells in the far-field also help dissipate any reflections. A no-slip condition was used at the solid surface, even though the boundary layer was not resolved due to computer limitations.

By using a set of faces that are actually used by the flow solver during the computation, there is no additional work required to extract the data needed for the far-field noise. This type of FW-H surface also reflects the true mesh clustering present where the flow variables are locally being computed: there is no loss in accuracy due to the interpolation onto a surface whose refinement might not be that of the computational grid. Since only the surface terms are evaluated during the acoustic prediction procedure, one does not have to take into account any phenomenon occurring outside the integration surface. The surface can also cross regions dominated by nonlinear effects.

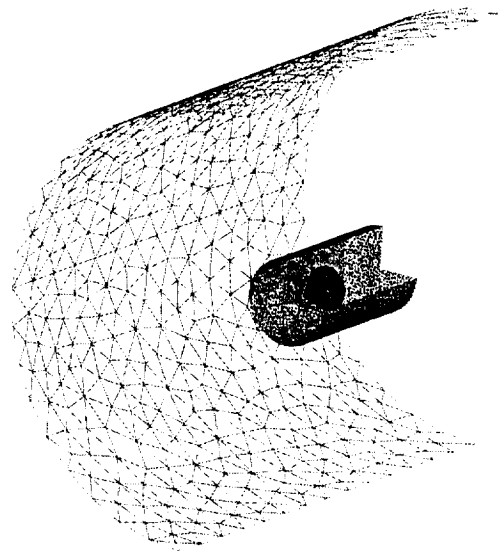

**Fig. 1 Overall view of the 280,000 cell mesh.**

During a run, the faces (triangles in this case) would be identified and flagged on each CPU, so that face data would be output at a prescribed sampling rate (around 50 kHz in the present case): the sampling was done in such a manner that one had at least 20 data points per wavelength, the shortest wavelength being 10 times that of the simulated shedding frequency. To avoid any redundant data, faces shared between two adjacent CPUs had to be identified at the beginning of each run, so that the number of faces whose data are output is identical to the number of triangles on the actual FW-H surface. The grid partitioning being done dynamically each time a run is initialized, the global cell indexing changes from run to run, making it necessary to run the above flagging procedure any time the program is restarted. This makes the routine independent of the number of CPUs being used. Figure 2 illustrates the regions on the surface shared between 8 processors using the Gibbs-Poole-Stockmeyer reordering algorithm.[5] As expected, each region is a neighbor to at most two other partitions, minimizing the amount of inter-processor communication.

The time step needed for a time-accurate solution is determined by the smallest cell characteristic length. This is estimated to be one third of the cell volume divided by the maximum face area. For the grid described above, this yields a time step of 9.45E-08 second at a CFL number of 0.9. The shedding frequency found during the experimental investigation of the flow is 36 Hz, for a Strouhal number equal to 0.171.

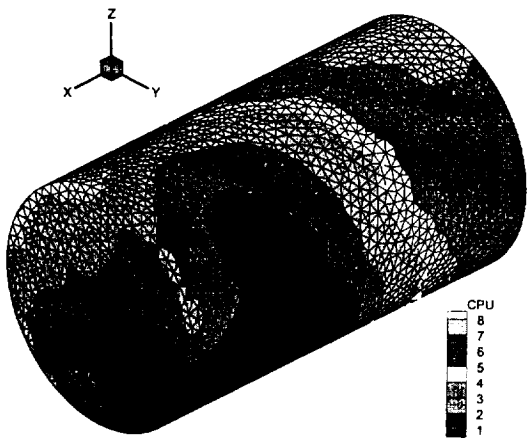


**Fig. 2 Partitioning of the FW-H surface across 8 processors.**

The Strouhal number was defined based on the cone diameter as $St = f_s d/U_\infty$. The numerical simulation is performed at Mach 0.2 at standard atmospheric pressure and temperature conditions, with an increased viscosity to match the experiment's Reynolds number (50,000). Scaling the Strouhal number to the simulation's Mach number yields a shedding frequency of 230 Hz. The computation of a complete shedding cycle requires roughly 46,000 iterations.

## The Flow Solver - PUMA

PUMA is a computer program, written in C, for the analysis of internal and external non-reacting compressible flows over arbitrary complex geometries. PUMA uses the Message Passing Interface (MPI) to run the code in parallel. It can be run on arbitrary number of processors with very good scaling performance. Several papers[2,4] detail the benchmarking of the performance, and validation of PUMA.

PUMA is based on finite volume methods and supports mixed topology unstructured grids composed of tetrahedra, wedges, pyramids and hexahedra. The code may be run to preserve time accuracy for unsteady problems, or may be run using a pseudo-unsteady formulation to enhance the convergence to the steady state. Primitive flow quantities are computed at the cell centers. The code can be restarted from any point of time at which the solution is available from previous computations. All flow variables are stored with double precision, but may be optionally stored as single precision to save memory and communication time at the cost of reduced precision.

## Parallel Machines

Computational Aeroacoustics (CAA) codes are usually very computationally intensive. Even with very powerful machines, such jobs may require days, or even months to give results. Parallel computing using Beowulf clusters offers an inexpensive way to handle such time-consuming simulations in reasonable amount of time.

Three facilities offering parallel computational power at Penn State were used for the computations - COst effective COmputing Array (COCOA),[2] COCOA2 and LionX.[6] COCOA is a Beowulf cluster comprising of 25 machines each having dual 400 MHz Pentium II processor. This facility was assembled by the authors and their colleagues in the Department of Aerospace Engineering at Penn State. The machines are connected via fast-Ethernet network which can support up to 100 Mbps bandwidth. A single Baynetworks 24-port fast-Ethernet switch with a backplane bandwidth of 2.5 Gbps is used for the networking. All the processors are dedicated to run parallel jobs. The operating system is Red Hat Linux. Message Passing Interface (MPI) is used for parallel programming and the Gnu C compiler is used for compiling PUMA. Details regarding setting up and benchmarking of COCOA may be obtained from Modi and Long[2] and COCOA's website.[7]

COCOA was primarily set up to make parallel computing facility readily available to the CFD group of the Aerospace Engineering Department at Pennsylvania State University. The total cost of the cluster was just $80,000 in the year 1998, when it was set up. Since then this facility has been intensively used for various CFD simulations. COCOA2 is a newly assembled Beowulf cluster at Penn State. It has 21 nodes each having dual 800 MHz Pentium III processors and 1 GB RAM each. The cluster has dual fast-Ethernet per node and all the nodes are connected using two HP2524 switches with channel bonding.

Figure 4 plots the parallel speedup for COCOA and COCOA2 (1 Mflop = one million floating point operations per second). Fairly good performance is obtained considering the small size of the problem. Figure 4 shows the reduction in the flop rate per processor as the grid points are distributed over a larger number of processors. This trend is typical of Beowulf clusters as the ratio of computation over communication decreases.

LionX is also a Beowulf cluster with 32 machines (each having dual 400 MHz Intel Xeon processors). These machines are connected via Myricom Myrinet with wire speed 1.28 Gbps. LionX also uses Linux with MPI for parallel programming. Performance comparison and benchmarking results for LionX can be obtained from its website.[6]

## CFD Results

After initializing all variables to the freestream values, local time stepping is used to accelerate the convergence towards a physically realistic flow. This is

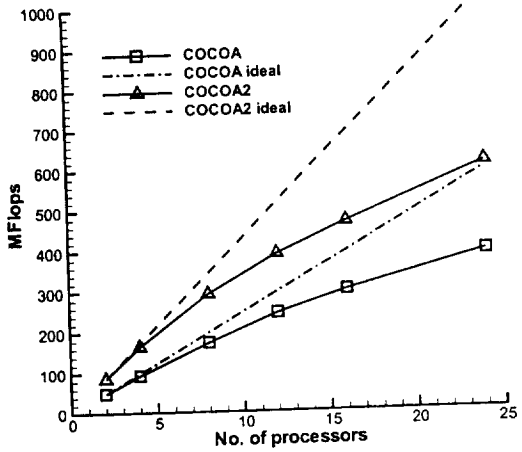


**Fig. 3 Parallel speed up for COCOA and COCOA2**

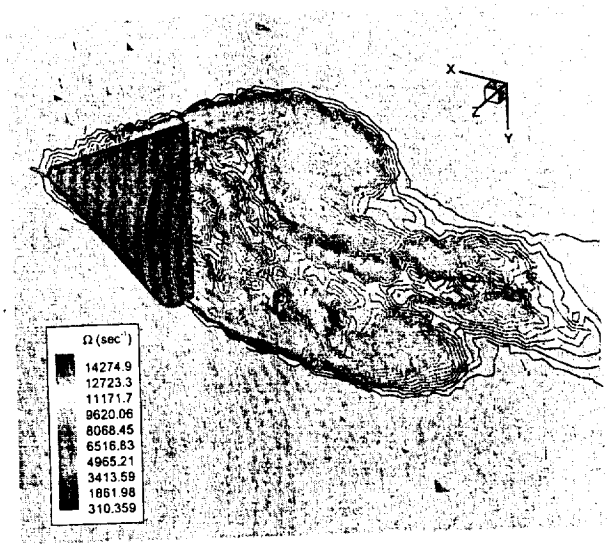


**Fig. 5 Instantaneous vorticity contours.**

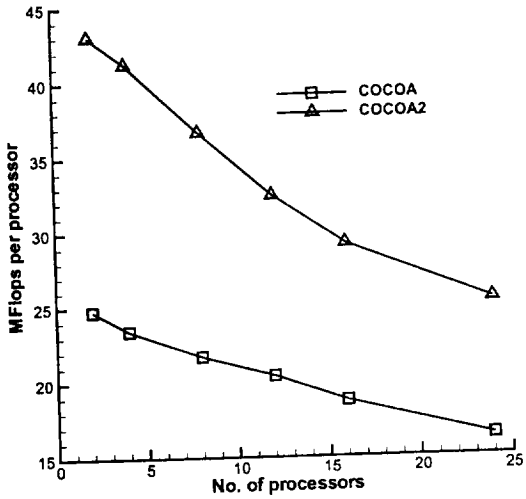


**Fig. 4**

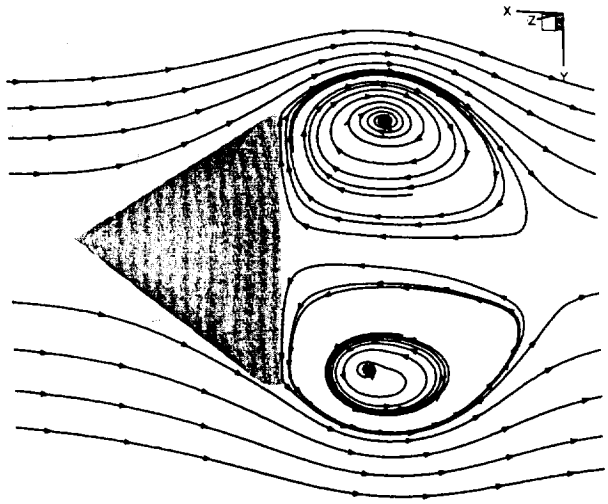

**Fig. 6 Average streamlines over one shedding cycle.**

done by assigning to each cell the maximum allowable time step for a given CFL number based on each cell characteristic cell length. Global time stepping is then turned on for several cycles before data are sampled, to ensure that the data on the FW-H surface follow the equations of motion. Figure 5 illustrates the vorticity patterns in the wake of the cone, showing strong recirculation phenomena. The noise from this recirculation is predicted by the FW-H module. Figure 6 is the averaged streamline contour over one shedding period, illustrating the axisymmetric bubble that was observed during Calvert's experimental study.[8]

In order to validate the solution, multiple comparisons were made between the simulation and the experimental measurements. A basic Smagorinksy sub-grid scale turbulence model[9] was added to the flow solver in order to improve the predictions, since a large-eddy simulation should yield better turbulent quantities.

Figure 7 shows the averaged streamwise velocity profiles computed by the original flow solver and those computed by the same solver combined with an LES. In all three cases the magnitude of the reverse flow velocity is under predicted when compared with experimental measurements. The predictions agree fairly well with Calvert's data in terms of the length of the recirculation zone. Past the stagnation point, the results including LES modeling follow the experimental curve more closely than those computed without any turbulence model.

Figure 8 illustrates the variation of the pressure coefficient $C_p$ along the wake centerline. In this case, the LES having the largest sub-grid scale constant $C_s$ greatly over-corrects the pressure drop in the near wake of the cone. The LES using a Smagorinsky constant of 0.10 matches the measured pressure data

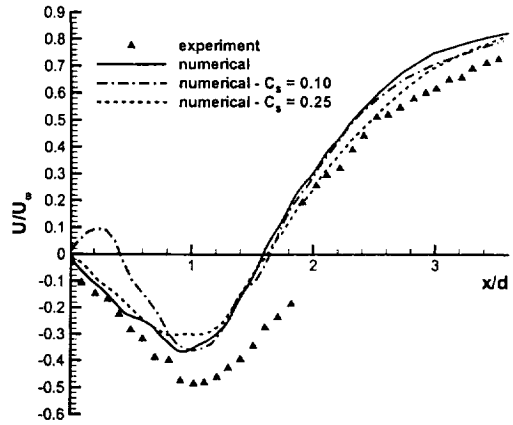


**Fig. 7 Comparison of the averaged streamwise velocity with experiments for the flow solver with and without LES.**

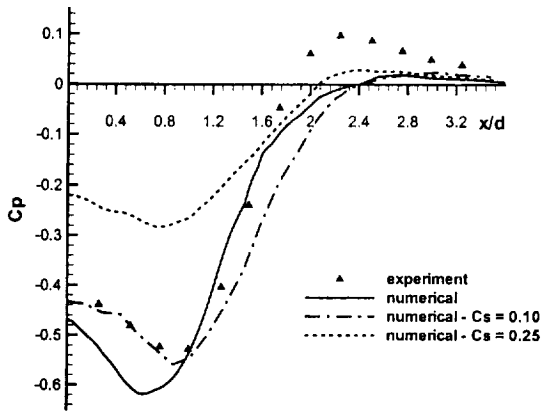


**Fig. 8 Comparison of the Cp coefficient with experiment for the flow solver with and without LES.**

very well until the stagnation point is reached. These results are consistent with those found in other related investigations, using either the $k$-$\epsilon$ turbulence model[10] or the $k$-$\epsilon$-$v^2$ model.[11] These simulations were compared against a set of experiments[12] at a lower Reynolds number (42,000). Madabhushi[13] also used an LES with as many as 850,000 mesh points, but completely over-predicted the length of the recirculation zone.

Figure 9 shows that the averaged streamwise perturbation velocity is not well predicted using any of the sub-grid scale constants. With the grid coarsening in the far wake, the fluctuating velocities are damped very rapidly as one goes away from the cone base. It is the flow solver without any turbulence model that

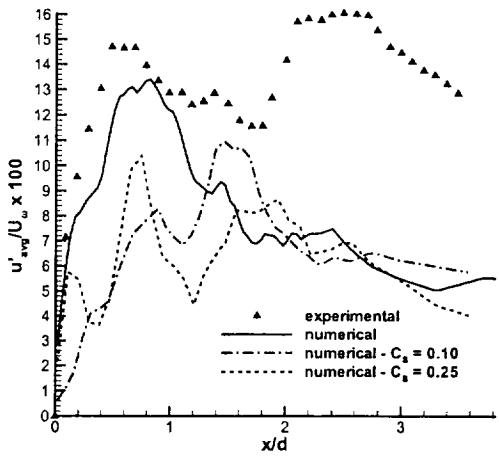


**Fig. 9 Comparison of averaged streamwise perturbation velocity with experiments with and without LES.**

yields unsteady velocity values that are closest to the experimental data. The solution without LES was selected to try to predict the far-field noise. It also leads to the conclusion that a more advanced turbulence model (dynamic LES, Detached Eddy Simulation) is needed to simulate such separated flows, as found in Strelets.[14]

## Far-Field Noise Prediction

The two commonly used methods for far-field aerodynamic noise predictions use the Kirchhoff equation or the Ffowcs Williams-Hawkings (FW-H) equation. While the governing equation in the 'moving surface' Kirchhoff formulation[15] is a convective wave equation, the FW-H equation is an exact rearrangement of the continuity and the momentum equations into the form of an inhomogeneous wave equation. Therein lies the strength of the FW-H equation over the Kirchhoff formulation. The FW-H equation gives accurate results even if the surface of integration lies in the nonlinear flow region. This is typically the case in jets and wakes when the nonlinear region extends to large distances downstream.

In the Kirchhoff formulation the source terms are assumed to be distributed over a fictitious surface in the flow. The nonlinear effects (nonlinear wave propagation and steepening; variations in the local sound speed; and noise generated by shocks, vorticity, and turbulence in the flow field) happening within the Kirchhoff surface are captured by the surface integration terms, but the Kirchhoff formulation requires the integration surface to be placed in a linear flow region (i.e. far away from the body). This is difficult to achieve as most computational grids are generated with the concern of minimizing computations. Usually, a fine quality mesh is used near the body with increas-

ing cell size towards the outer boundaries. Therefore, the quality of the solution available in the linear flow region is generally bad. The FW-H equation, on the other hand, works fine even if the integration surface is in the nonlinear flow region. A detailed comparison of the Kirchhoff and FW-H formulations is provided in Brentner and Farassat.[16]

The solution of the full FW-H equation requires the evaluation of two surface integrals and one volume integral. The surface integrations correspond to the "thickness" noise (monopole) and the "loading" noise (dipole). The volume integration corresponds to the quadrupole term which accounts for the nonlinearity in the flow.[15,17] Evaluating the volume integral can be extremely computationally intensive and difficult to implement. Fortunately, the quadrupole term can be safely ignored for most subsonic flows as is the case in the present study.

Only recently has the FW-H equation been used on a fictitious (i.e. not the same as the body) permeable integration surface[18] - exactly like the Kirchhoff approach. di Francescantonio[18] demonstrated that when the FW-H approach is applied on a Kirchhoff-type surface, the quadrupole sources enclosed within the surface are accounted for by the surface sources. It should be noted that the "thickness" noise and the "loading" noise as obtained from solving FW-H equation do not have any physical significance if the surface of integration is chosen to be permeable (fictitious). However, when the integration surface coincides with the body, these terms provide a physical insight into the source of sound generation.

The FW-H equation is written in the standard differential form as

$$\begin{aligned} \Box^2 p'(\mathbf{x},t) &= \frac{\partial^2}{\partial x_i \partial x_j}\left[T_{ij}H(f)\right] \\ &- \frac{\partial}{\partial x_i}\left[L_i\delta(f)\right] + \frac{\partial}{\partial t}\left[(\rho_o U_n)\delta(f)\right] \end{aligned} \quad (1)$$

where $L_i$ and $U_n$ are defined as

$$\begin{aligned} U_n = U_i\hat{n}_i \;::\; U_i &= (1-\frac{\rho}{\rho_o})v_i + \frac{\rho u_i}{\rho_o} \\ L_i &= P_{ij}\hat{n}_j + \rho u_i(u_n - v_n) \end{aligned} \quad (2)$$

and $T_{ij}$ is the Lighthill stress tensor. The FW-H equation can be solved using the formulation in Brentner and Farassat,[16] and the solution can be written in an integral form as

$$\begin{aligned} 4\pi p'(\mathbf{x},t) &= \int_{f=0}\left[\frac{\rho_0(\dot{U}_n + U_{\dot{n}}) + \dot{L}_r/c}{r(1-M_r)^2}\right]_{ret} \mathrm{d}S \\ &+ \int_{f=0}\left[\frac{(\rho_0 U_n + Lr/c)(r\dot{M}_r + c(M_r - M^2))}{r^2(1-M_r^3)}\right]_{ret} \mathrm{d}S \\ &+ \int_{f=0}\left[\frac{L_r - L_M}{r^2(1-M_r)^2}\right]_{ret} \mathrm{d}S \end{aligned} \quad (3)$$

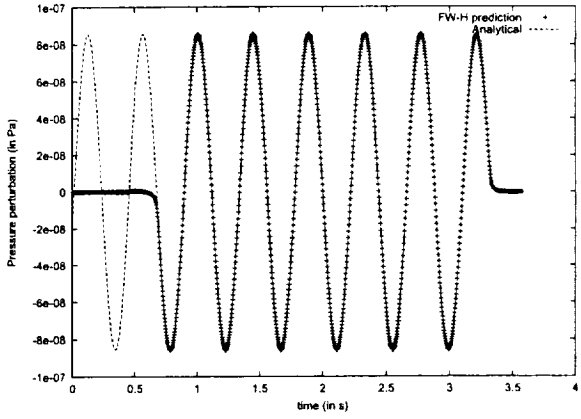


**Fig. 10 Validation of the FW-H code against the analytical solution for a stationary monopole in a uniform mean flow.**

The quadrupole term is ignored in the present formulation. The integrations are performed on the FW-H surface at retarded time. Since the FW-H surface is fixed relative to the body (the cone) for this study, and the flow Mach number is constant, the following terms in the above integrals are zero : $U_{\dot{n}} = \dot{M}_r = 0$. The standard time binning technique discussed by Özyörük and Long[19] is used for obtaining pressure at the observer locations.

## The FW-H code and its Validation

The FW-H code is written in Fortran 90. The code was tested for a model problem - a stationary monopole in a uniform mean flow. The FW-H surface is chosen to be a box made up of rectangular panels. The analytical solution to the model problem is evaluated at the center of each panel to obtain the time history of the primitive variables on the FW-H surface. The prediction from the FW-H code (using the analytical data on the surface as input) is then compared with the analytical pressure perturbation at a point outside the surface. Figure 10 compares at an arbitrary point (300 m, 0, 0) the pressure perturbation predicted by the FW-H code and that obtained analytically for a stationary monopole source with an amplitude of 0.01 Pascals and a frequency of 2.267 Hz placed in a uniform mean flow of 0.3 Mach number. The analytical solution to this problem is :

$$\begin{aligned} \phi(\mathbf{x},t) &= \frac{\epsilon\,\exp(i\omega\tau_*)}{4\pi\left[(x+\mathrm{U}_0(\tau_*-t))^2+y^2+z^2\right]^{1/2}} \\ &\times \frac{1}{1+\frac{\mathrm{M}_0(x+\mathrm{U}_0(\tau_*-t))}{\left[(x+\mathrm{U}_0(\tau_*-t))^2+y^2+z^2\right]^{1/2}}} \end{aligned} \quad (4)$$

where $\tau_*$ is given by

$$\tau_* = t + \frac{\mathrm{M}_0 x - \left[(x^2+(1-\mathrm{M}_0{}^2)(y^2+z^2)\right]}{c(1-\mathrm{M}_0{}^2)} \quad (5)$$

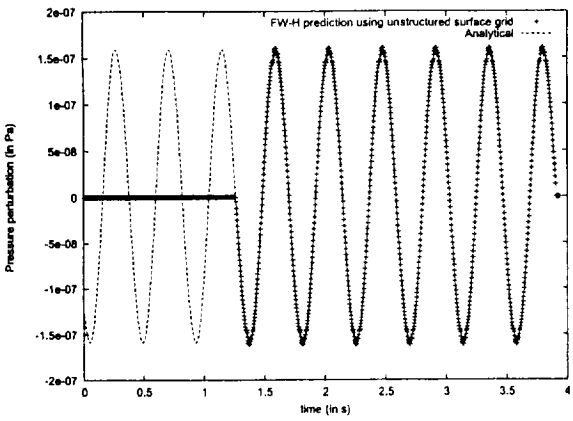


**Fig. 11 Comparison of the FW-H prediction using unstructured surface grid against the analytical solution.**

The unstructured grid over the cone is created such that there is an unstructured cylindrical surface enclosed in the computational domain (Fig. 1). This surface is chosen to be the permeable FW-H surface. The elements of the surface are faces of the tetrahedra, and therefore, triangles. Since these triangles are chosen from the unstructured mesh, the area and normal varies from element to element. This, however, is not a problem because the FW-H equation only requires information on a closed surface; it does not depend on the structure of the elements constituting the surface. Clustering of the surface elements is desired to increase the resolution of the sources. The FW-H surface used for the present computation is the inner cylinder in Fig. 1. This grid was used with the model problem of stationary monopole in a uniform mean flow to test if the unstructured grid poses any problems. A perfect match is observed between the FW-H prediction and the analytical solution (Fig. 11). The comparison is made at an aribtrary point (300 m, 0, 0). This confirms that an unstructured-mesh surface can be used as a FW-H surface without any loss of accuracy. Note that the first few seconds where the FW-H prediction does not match the analytical solution is the time it takes for the sound to reach the observer. This delay is more in Fig. 11 than in Fig. 10 because the unstructured FW-H surface is very small and hence, farther away from the observer point than the structured surface used for Fig. 10.

## Results for the Cone

PUMA is used to obtain time accurate data (the primitive flow variables) on the FW-H surface. One complete shedding cycle of the simulation is used for far-field noise prediction. Pressure at a few points outside the FW-H surface (in the near field) is collected to compare with the predictions of the FW-H code. Four points distributed in the azimuthal direction near the base of the cone and very close to but outside the FW-H surface were chosen for comparison. The coordinates of the points are tabulated in Table 1. The cone has a base diameter of 0.02 m and a vertex angle of 60°. The center of the base of the cone is at the origin and the vertex points upstream (positive x). The FW-H surface is a cylinder of radius 0.05 m and length 0.175 m, centered at the origin.

| Point No. | x (m) | y (m) | z (m) |
|---|---|---|---|
| 1 | 0 | -0.055 | 0 |
| 2 | -0.025 | 0.055 | 0 |
| 3 | 0 | 0 | 0.05 |
| 4 | 0 | 0 | -0.055 |

**Table 1 Coordinates of the observer locations for comparing FW-H predictions against PUMA.**

Figure 12 compares the pressure fluctuations at the four points listed in Table 1. Note that the PUMA pressure predictions have been shifted up by 20 Pascals. This is relatively a very small amount, about 0.02% of the mean pressure. We believe that this under-prediction by PUMA may be due to the dissipation caused by inadequate clustering of grid cells. It may also be due to the small sample size, and we plan to do ensemble averaging. Note that this error is of the order of magnitude of pressure pertubations predicted by the FW-H code at any point inside the FW-H surface, which should actually be zero. However, the prediction by the FW-H code agrees very well qualitatively with the PUMA solution.

## Sound Directivity

The directivity of the noise from the cone was obtained by calculating the root mean squared (r.m.s.) pressure perturbation for one shedding cycle at different observer locations in azimuthal and longitudinal directions. Since the calculation for one observer location is completely independent of any other location, it is a perfect problem to run in parallel. Long and Brentner[20] suggested some self-scheduling parallel methods for multiple serial codes. However, no parallalization was done for the noise prediction results presented here.

Figure 13 plots the directivity pattern in the azimuthal direction on the plane $x = -0.1$ m, which is right behind the base of the cone. The pattern in Fig. 13 is symmetric because of the symmetry of the cone about its axis. Since the FW-H equation cannot predict the pressure fluctuation inside the FW-H surface, we can compute the noise only outside the FW-H surface. Therefore, the directivity patterns are plotted in an annular region outside the FW-H surface.

Figure 14 plots the directivity pattern in the longitudinal direction on the $z = 0$ plane. Since the noise is caused by both turbulence and fluctuating surface forces, the directivity shows several lobes.

A conventional polar directivity pattern in the longitudinal direction ($z = 0$ plane) is plotted in Fig. 15

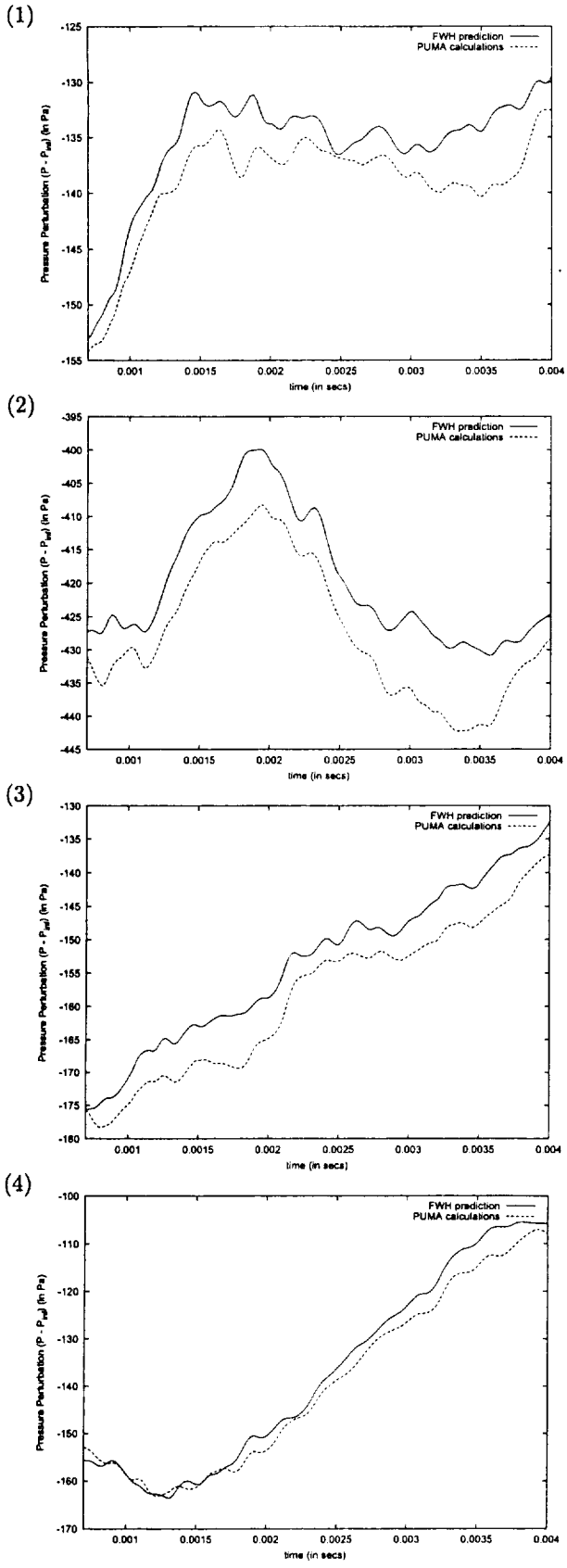


**Fig. 12 Comparison of pressure fluctuation, $p - p_\infty$ as predicted by PUMA and FW-H code at various locations listed in Table 1.**

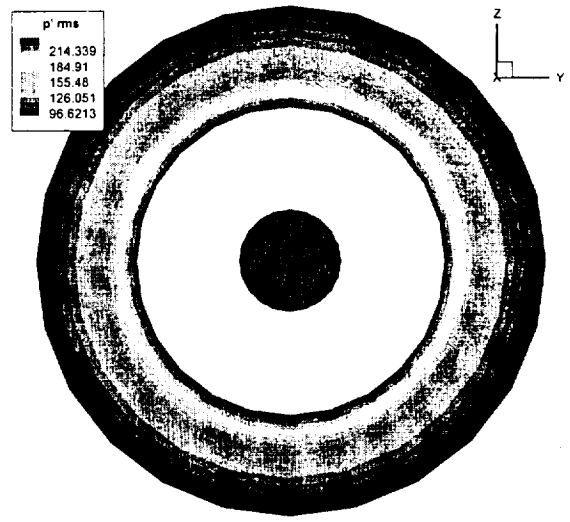


**Fig. 13 Directivity of the noise in the azimuthal direction behind the base of the cone ($x = -0.1$).**

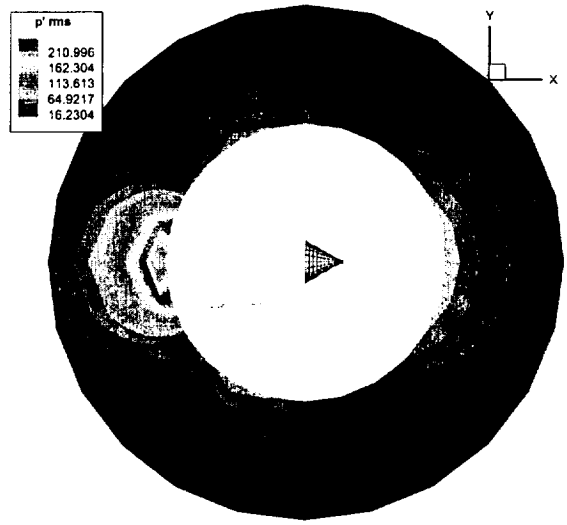


**Fig. 14 Directivity of the noise in the longitudinal direction in the plane $z = 0$.**

for observers at 10 different radial locations ($r = 0.15$ - 0.24 m). In Fig. 15, the cone is pointing to the right; the radial distance from the origin is equal to the r.m.s. pressure and the angle (theta) illustrates the location of the observer point in the domain.

## Conclusions

Aerodynamic noise from a cone has been studied as a model problem to test the possibility of using unstructured grids for noise prediction from complicated bodies like landing gears, slats etc. A finite volume flow solver, PUMA has been used to obtain time-accurate flow data on a permeable FW-H surface. The FW-H code was validated against a model problem of a monopole in a uniform mean flow. The predictions from the FW-H code have been compared

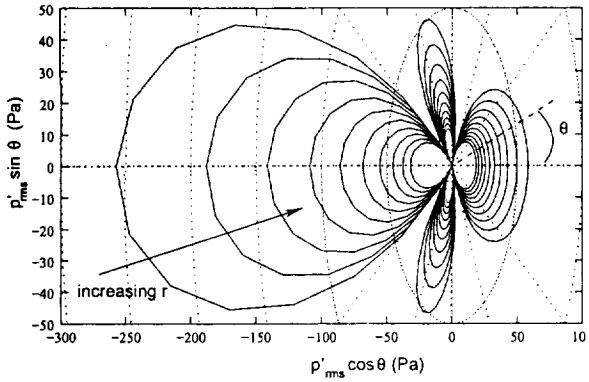


**Fig. 15 Polar plot of sound directivity in $z = 0$ plane at a few radial locations.**

at four observer locations in the near field with direct calculations from PUMA. Noise predictions are made for a period of one shedding cycle. The comparison is fairly accurate with only a small D.C shift error. The directivity patterns of the noise from the cone are plotted in azimuthal and longitudinal directions. The sound directivity pattern has been shown to be fairly complicated due to the complex physics inside the FW-H surface.

# References


[1]Bruner, C. W. S. and Walters, R. W., "Parallelization of the Euler Equations on Unstructured Grids," AIAA Paper 1997-1894, 35th Aerospace Sciences Meeting, Jan. 1997.

[2]Modi, A. and Long, L. N., "Unsteady Separated Flow Simulations using a Cluster of Workstations," Paper 2000-0272, $38^{th}$ Aerospace Sciences Meeting & Exhibit, Jan. 2000.

[3]Sharma, A. and Long, L. N., "Airwake Simulations on LPD 17 Ship," Paper 2001-2589, $31^{st}$ AIAA Fluid Dynamics Conference and Exhibit, Anaheim, California, 2001.

[4]Modi, A., *Unsteady Separated Flow Simulations using a Cluster of Workstations*, M.S. dissertation, The Pennsylvania State University, Department of Aerospace Engineering, May 1999.

[5]I. S. Duff, A. M. E. and Reid, J. K., *Direct Methods for Sparse Matrices*, Oxford University Press, 1986.

[6]http://cac.psu.edu/beatnic/Cluster/Lionx/perf.

[7]http://cocoa.ihpca.psu.edu.

[8]Calvert, J. R., "Experiments on the Low-Speed Flow Past Cones," *Journal of Fluid Mechanics*, Vol. 27, 1967, pp. 73–289.

[9]Smagorinsky, J., "General Circulation Experiments with the Primitive Equations," *Monthly Weather Review*, Vol. 91, 1963, pp. 99–165.

[10]S. H. Johansson, L. D. and Olsson, E., "Numerical Simulation of Vortex Shedding Past Triangular Cylinders at High Reynolds Number Using a $k$-$\epsilon$ Turbulence Model," *International Journal For Numerical Methods in Fluids*, Vol. 16, 1993, pp. 859–878.

[11]Durbin, P. A., "Separated Flow Computations with the $k$-$\epsilon$-$v^2$ Model," *AIAA Journal*, Vol. 33, No. 4, 1995, pp. 659-670.

[12]A. Sjunnesson, C. N. and Max, E., "LDA Measurements of Velocities and Turbulence in a Bluff Body Stabilized Flame," *Laser Anemomatry*, Vol. 3, 1991, pp. 83–90.

[13]R. K. Madabhushi, D. C. and Barber, T. J., "Unsteady Simulations of Turbulent Flow Behind a Triangular Bluff Body," paper 97-3182, $33^{r}d$ AIAA Joint Propulsion Conference and Exhibit, Seattle, WA, 1997.

[14]Strelets, M., "Detached Eddy Simulation of Massively Separated Flows," AIAA Paper 2002-0879, AIAA Aerospace Sciences Meeting and Exhibit, Reno, NV, 2001.

[15]Farassat, F. and Myers, M. K., "An Anaysis of the Quadrupole Noise Source in High Speed Rotating Blades," *Computational Acoustics - Scattering, Gaussian Beams, and Aeroacoustics*, Vol. 2, 1990, pp. 227–240.

[16]Brentner, K. S. and Farassat, F., "An Analytical Comparison of the Acoustic Analogy and Kirchoff Formulation for Moving Surfaces," *AIAA Journal*, Vol. 36, No. 8, Aug. 1998, pp. 1379–1386.

[17]Farassat, F., "Quadrupole Source in Prediction of Noise of Rotating Blades-A New Source Description," AIAA Paper 1987-2675, 1987.

[18]di Francescantonio, P., "A New Boundary Integral Formulation for the Prediction of Sound Radiation," *Journal of Sound and Vibration*, Vol. 202, No. 4, 1997, pp. 491–509.

[19]Özyörük, Y. and Long, L. N., "A New Efficient Algorithm for Computational Aeroacoustics on Parallel Procesors," *Journal of Computational Physics*, Vol. 125, 1996, pp. 135–149.

[20]Long, L. N. and Brentner, K. S., "Self-Scheduling Parallel Methods for Multiple Serial Codes with Application to WOPWOP," AIAA Paper 2000-0346, $38^{th}$ Aerospace Sciences Meeting & Exhibit, Reno, NV, 2000.

# Numerical Simulation of Subsonic Inviscid Flow past a Cone Using High-Order Finite Difference Schemes

Jae Wook Kim* and Philip J. Morris√

Department of Aerospace Engineering

The Pennsylvania State University

University Park, PA 16802

* Post-Doctoral Research Associate; currently, Research Professor, Department of Aerospace Engineering, Korea Advanced Institute of Science and Technology,

Taejon 305-701, Republic of Korea

√ Boeing/A.D. Welliver Professor, Associate Fellow AIAA

## Abstract

The wake-dominated unsteady subsonic flow of Mach number 0.2 past a cone of vertex angle 60° is calculated numerically using high-order finite difference schemes on structured grids. The three-dimensional compressible Euler equations are solved to simulate an inviscid flow that exhibits large fluctuations of pressure and velocity due to the shedding of vortices behind the cone. An axisymmetric structured grid system is used, that is generated by rotating a two-dimensional grid plane around a centerline. The grid singularity at the centerline, where the Jacobian and some grid metrics approach infinity, is avoided by changing the form of the flux vectors in the Euler equations without any asymptotic assumption or simplification. Fourth- and sixth-order finite difference schemes are used for the evaluation of spatial derivatives, and a fourth-order Runge-Kutta scheme is used for marching the solution in time. The complex wake motions behind the cone are investigated by visualizing the vorticity field. The mean flow pattern and periodic phenomena are analyzed and compared with the experimental data. This demonstrates the accuracy of the present approach to further analyses of wake-dominated flows past axisymmetric bluff bodies.

## I. Introduction

Calvert [1] studied experimentally the low-speed flow patterns and the associated periodic phenomena with flow past a cone of various vertex angles. He noted that there was little published work on incompressible flow past an axisymmetric blunt-based body, except some experiments carried out between the 1930's and 1960's. These earlier studies were restricted to flow visualization at low Reynolds numbers. He also discussed the periodic phenomena associated with such flows that are presumably related to some kind of regular vortex shedding: however, the actual wake pattern is unknown above a Reynolds number of a few hundred. Cal-

vert's measurements of mean and fluctuating velocity, and mean pressure for various cone angles show that the wakes are all similar. This problem has received little attention in either experimental or computational studies during the last three decades. Recently, Long *et al.* [2] performed a simulation of a cone wake flow using low-order finite volume methods on unstructured grids. The wake pattern and periodic phenomena in subsonic flow past a blunt-based body are of importance in the design of airframe components such as landing gears, especially for the reduction of aerodynamic noise: but, the existing knowledge of their flow characteristics is still far from complete. This paper seeks to provide some understanding of these complex flows through the simulation of the wake generated by an axisymmetric blunt-based cone.

The present paper focuses on the application of high-order finite difference schemes and structured grids to the computation of a three-dimensional, unsteady, inviscid, compressible flow past a cone at subsonic speeds. The scope of the present study is limited to the large scales of the wake turbulence and the shedding vortices, rather than the fine scales of turbulence whose simulation would demand huge computational resources and time. Therefore, the compressible Euler equations are used in the present computation. Fourth- and sixth-order numerical schemes, based on central finite differences, are used for the solution of the Euler equations. These methods have been developed for high accuracy and high resolution in the direct computation of unsteady flows and acoustics [3, 4]. In addition, an artificial dissipation model and time-dependent boundary conditions are combined with the high-order schemes for a long-time stable solution [5-7].

The solutions are produced in a structured grid system generated by rotating a two-dimensional grid plane around the axis of symmetry. The axisymmetric structured grid has a grid singularity at the centerline, where the Jacobian and some grid metrics approach infinity. When a conventional form of the Euler equations is considered, this singularity makes it hard to calculate the flux variables at the centerline and the flux derivatives near the centerline when wide differencing stencils are used across the centerline in a generalized coordinate system.

This paper proposes a way to avoid the centerline singularity by changing the form of the flux vectors in the Euler equations without any asymptotic assumption or simplification. In this way, all the flux variables and derivatives may be evaluated without loss of accuracy. The singularity treatment is a great help in the calculation of the flux derivatives near the centerline: however, the Euler equations are still indeterminate at the centerline. In the present approach, the solutions themselves at the centerline are interpolated from the neighboring values.

The problem conditions for the present computation are a free-stream Mach number of 0.2 and cone vertex angle of 60°. The present work provides a visualization of the wake flow field with its shedding vortices, and an analysis of the mean flow patterns and the periodic phenomena. The results are compared to Calvert's experimental data [1] for validation of the accuracy of the solution. A spiral pattern of the wake flow behind the cone is shown clearly through a visualization of the wake vorticity field. The initial location of the regular vortex shedding and its Strouhal number are simulated correctly. These successful comparisons indicate that the present methodology is capable of describing three-dimensional, unsteady, bluff-body wake flows.

In the next section, the governing equations and the treatment of the centerline singularity are described. The high-order finite difference schemes are then introduced. The grid, and initial and boundary conditions are then discussed. Both qualitative and quantitative results for the wake flow field and a comparison with experiment are then presented.

## II. Governing Equations and Centerline Singularity

The governing equations are the three-dimensional compressible Euler equations. The flux vector form of the Euler equations transformed to the computational domain may be expressed in generalized coordinates as,

$$\frac{\partial \hat{\mathbf{Q}}}{\partial t}+\frac{\partial \hat{\mathbf{E}}}{\partial \xi}+\frac{\partial \hat{\mathbf{F}}}{\partial \eta}+\frac{\partial \hat{\mathbf{G}}}{\partial \zeta}=\hat{\mathbf{0}} \tag{1}$$

where the flux vectors in generalized coordinates may be represented as

$$\hat{\mathbf{Q}}=\frac{\mathbf{Q}}{J},\quad \hat{\mathbf{E}}=\frac{1}{J}\left(\xi_x\mathbf{E}+\xi_y\mathbf{F}+\xi_z\mathbf{G}\right),\quad \hat{\mathbf{F}}=\frac{1}{J}\left(\eta_x\mathbf{E}+\eta_y\mathbf{F}+\eta_z\mathbf{G}\right),\quad \hat{\mathbf{G}}=\frac{1}{J}\left(\zeta_x\mathbf{E}+\zeta_y\mathbf{F}+\zeta_z\mathbf{G}\right). \tag{2}$$

The conservative variables and the flux vectors in Cartesian coordinates are given by

$$\mathbf{Q}=\begin{bmatrix}\rho\\ \rho u\\ \rho v\\ \rho w\\ \rho e_t\end{bmatrix},\quad \mathbf{E}=\begin{bmatrix}\rho u\\ \rho u^2+p\\ \rho vu\\ \rho wu\\ (\rho e_t+p)u\end{bmatrix},\quad \mathbf{F}=\begin{bmatrix}\rho v\\ \rho uv\\ \rho v^2+p\\ \rho wv\\ (\rho e_t+p)v\end{bmatrix},\quad \mathbf{G}=\begin{bmatrix}\rho w\\ \rho uw\\ \rho vw\\ \rho w^2+p\\ (\rho e_t+p)w\end{bmatrix}$$

where the total energy per unit mass is defined as $e_t=p/[(\gamma-1)\rho]+(u^2+v^2+w^2)/2$ and $\gamma=c_p/c_v$ is the ratio of specific heats. $\gamma=1.4$ in the present computation. In the Eq. (2), the transformation Jacobian, $J$ and the grid metrics, $\xi_x,\cdots,\zeta_z$ are given by

$$J=\frac{1}{x_\xi(y_\eta z_\zeta-y_\zeta z_\eta)+x_\eta(y_\zeta z_\xi-y_\xi z_\zeta)+x_\zeta(y_\xi z_\eta-y_\eta z_\xi)}, \tag{3}$$

with,

$$\begin{bmatrix}\xi_x & \xi_y & \xi_z\\ \eta_x & \eta_y & \eta_z\\ \zeta_x & \zeta_y & \zeta_z\end{bmatrix}=J\begin{bmatrix}y_\eta z_\zeta-y_\zeta z_\eta & z_\eta x_\zeta-z_\zeta x_\eta & x_\eta y_\zeta-x_\zeta y_\eta\\ y_\zeta z_\xi-y_\xi z_\zeta & z_\zeta x_\xi-z_\xi x_\zeta & x_\zeta y_\xi-x_\xi y_\zeta\\ y_\xi z_\eta-y_\eta z_\xi & z_\xi x_\eta-z_\eta x_\xi & x_\xi y_\eta-x_\eta y_\xi\end{bmatrix}. \tag{4}$$

In an axisymmetric structured grid, the Jacobian approaches infinity at the centerline and the denominator in Eq. (3) becomes zero. Therefore, all the grid metrics expressed in Eq. (4) are indeterminate at the centerline. However, one may easily show that the ratios of the grid metrics to the Jacobian remain finite or zero at the centerline, even though the Jacobian and some grid metrics themselves have infinite values. This suggests a way to remove the centerline singularity. The key is to choose a different way of expressing the Jacobian and the grid metrics. New variables that replace the conventional Jacobian and the grid metrics are defined by

$$J^* \equiv \frac{1}{J} = x_\xi(y_\eta z_\zeta - y_\zeta z_\eta) + x_\eta(y_\zeta z_\xi - y_\xi z_\zeta) + x_\zeta(y_\xi z_\eta - y_\eta z_\xi), \tag{5}$$

and

$$\begin{bmatrix} \xi_x^* & \xi_y^* & \xi_z^* \\ \eta_x^* & \eta_y^* & \eta_z^* \\ \zeta_x^* & \zeta_y^* & \zeta_z^* \end{bmatrix} \equiv \frac{1}{J} \begin{bmatrix} \xi_x & \xi_y & \xi_z \\ \eta_x & \eta_y & \eta_z \\ \zeta_x & \zeta_y & \zeta_z \end{bmatrix} = \begin{bmatrix} y_\eta z_\zeta - y_\zeta z_\eta & z_\eta x_\zeta - z_\zeta x_\eta & x_\eta y_\zeta - x_\zeta y_\eta \\ y_\zeta z_\xi - y_\xi z_\zeta & z_\zeta x_\xi - z_\xi x_\zeta & x_\zeta y_\xi - x_\xi y_\zeta \\ y_\xi z_\eta - y_\eta z_\xi & z_\xi x_\eta - z_\eta x_\xi & x_\xi y_\eta - x_\eta y_\xi \end{bmatrix}. \tag{6}$$

The new variables with a superscript asterisk defined in Eqs. (5) and (6) have finite or zero values in the entire computational domain, including at the centerline. Using the new variables, the expressions for the flux vectors given by Eq. (2) become

$$\hat{\mathbf{Q}} = J^*\mathbf{Q}, \quad \hat{\mathbf{E}} = \xi_x^*\mathbf{E} + \xi_y^*\mathbf{F} + \xi_z^*\mathbf{G}, \quad \hat{\mathbf{F}} = \eta_x^*\mathbf{E} + \eta_y^*\mathbf{F} + \eta_z^*\mathbf{G}, \quad \hat{\mathbf{G}} = \zeta_x^*\mathbf{E} + \zeta_y^*\mathbf{F} + \zeta_z^*\mathbf{G}. \tag{7}$$

In this manner, the centerline singularity is removed and all the flux variables at the centerline may be evaluated. Especially, this treatment of the singularity benefits the calculation of the flux derivatives in Eq. (1) near the centerline when using wide differencing stencils across the centerline. However, the Euler equations still cannot be solved at the centerline since $J^*$ is zero there and the vector of the conservative variables $\hat{\mathbf{Q}}$ vanishes from Eq. (7). This means that Eq. (1) becomes indeterminate and it is impossible to integrate the solutions in time. However, the solutions (conservative variables) at the centerline may be interpolated from the neighboring values.

## III. High-Order Finite Difference Schemes

High-order finite difference schemes with high-resolution characteristics are used in the present computation on a structured grid. The main scheme is a pentadiagonal type of central compact finite difference scheme [3, 4]. It is a generalization of the seven-point stencil Padé scheme used on the interior nodes. It may be expressed as

$$\beta f'_{i-2} + \alpha f'_{i-1} + f'_i + \alpha f'_{i+1} + \beta f'_{i+2} = \frac{1}{h} \sum_{m=1}^{3} a_m (f_{i+m} - f_{i-m}) \tag{8}$$

where $f_i$ is an objective function for the flux variables and $f'_i$ is its spatial derivative on the $i$-th node. The grid spacing $h$ is a constant independent of the index $i$ in the computational domain where all the grid points are equally spaced. Equation (8) may be solved by inverting a pentadiagonal matrix. The matrix must be completed at the boundaries. Therefore, non-central or one-sided formulations other than Eq. (8) are needed on the boundary and the near-boundary nodes to complete the matrix. These may be expressed as

$$f'_0 + \alpha_{0,1} f'_1 + \beta_{0,2} f'_2 = \frac{1}{h} \sum_{\substack{m=0 \\ m \neq 0}}^{3} a_{0,m} (f_m - f_0) \quad \text{for } i=0 \text{ (boundary node)}, \tag{9}$$

$$\alpha_{1,0} f'_0 + f'_1 + \alpha_{1,2} f'_2 + \beta_{1,3} f'_3 = \frac{1}{h} \sum_{\substack{m=0 \\ m \neq 1}}^{4} a_{1,m} (f_m - f_1) \quad \text{for } i=1, \tag{10}$$

$$\beta_{2,0} f'_0 + \alpha_{2,1} f'_1 + f'_2 + \alpha_{2,3} f'_3 + \beta_{2,4} f'_4 = \frac{1}{h} \sum_{\substack{m=0 \\ m \neq 2}}^{5} a_{2,m} (f_m - f_2) \quad \text{for } i=2. \tag{11}$$

The coefficients in Eqs. (8)-(11) are listed in Table 1. They are optimized, as described in Refs. 3 and 4, to achieve maximum resolution characteristics with fourth-order accuracy (second-order in Eq. (9) for numerical stability). The optimized fourth-order compact finite difference schemes are used to evaluate the flux derivatives in the mean flow and radial directions. On the other hand, the flux derivatives in the azimuthal direction are calculated with a conventional central finite difference scheme for a simple handling of the periodic condition across the branch cut. The standard central finite difference scheme is given by

$$f'_i = \frac{45(f_{i+1} - f_{i-1}) - 9(f_{i+2} - f_{i-2}) + (f_{i+3} - f_{i-3})}{60h}. \tag{12}$$

Equation (12) has sixth-order accuracy, which is the highest order of truncation for the given

standard seven-point stencil. Combined with the high-order finite difference schemes in space, the classical fourth-order four-stage Runge-Kutta scheme is used for marching the solutions in time.

As mentioned in Section II, the solutions (conservative variables) are obtained at the centerline not by solving the governing equations but by interpolation from the neighboring solutions. In the present work, a fourth-order interpolation is used at the centerline. It may be written as

$$f_0 = \frac{13(f_1 + f_{-1}) + 8(f_2 + f_{-2}) - 5(f_3 + f_{-3})}{32} \tag{13}$$

where the negative indexes mean the values in the opposite direction across the centerline. Actually, there are as many sets of the centerline solutions interpolated by Eq. (13) as half the number of grid points in the azimuthal direction. A unique value of the centerline solution is finally acquired by averaging these values.

High-order schemes in space and time resolve a wider range of wavenumber or frequency than low-order methods. However, even the present schemes do not resolve the high wavenumber or frequency range effectively, an adaptive nonlinear artificial dissipation model [6] is also used to remove the unwanted numerical oscillations that may develop from the unresolved range. The artificial dissipation model is implemented only at the last (fourth) stage of the Runge-Kutta scheme in order to minimize computational costs. In addition to the stringent requirements on the high-order and high-resolution numerical schemes, an accurate and robust calculation depends heavily on the suppression of any waves that may result from unwanted reflections on computational boundaries. The boundary conditions for a time-dependent problem should be physically correct and numerically well posed. Generalized characteristic boundary conditions [7] are used as the time-dependent boundary conditions in the present computation. Non-reflecting inflow/outflow and the inviscid wall conditions are imposed at the

boundaries of the computational domain and the cone surface respectively.

The accuracy of the high-order compact finite difference schemes, the adaptive nonlinear artificial dissipation model and the generalized characteristic boundary conditions has been validated through the previous publications of Refs. 3 to 7. They were applied to multi-dimensional steady/unsteady and inviscid/viscous computations in the various benchmark problems: linear wave convection in Ref. 3, acoustic radiation from axisymmetric baffle in Ref. 4, noise generation from airfoils in Ref. 5, shock-sound interaction in a transonic nozzle in Ref. 6, and wake flow and acoustic radiation from a circular cylinder in Ref. 7. It was shown that they produced very accurate numerical solutions in comparison with analytic solutions and experimental data. They can be used effectively in the present computation.

## IV. Procedure and Results of Numerical Simulation

In this section, the numerical simulation of an unsteady inviscid compressible flow past a cone of vertex angle 60° in a subsonic speed of Mach number 0.2 is described. The simulation uses high-order finite difference schemes and the modified form of the flux vectors in the Euler equations, in order to eliminate the centerline singularity.

### A. Grid System and Computation Procedure

For the present problem, the computational domain consists of two blocks and rotating a two-dimensional grid plane around the centerline as shown in Figs. 1 and 2 produces an axi-symmetric grid system. The number of grid planes in the azimuthal direction is 48. The number of grid points is 101×50×48 in block 1 and 161×51×48 in block 2. This gives a total of 636,528 grid points. The grid points are clustered along the centerline and near the edge of the cone base. The minimum grid size at the center of the base is $\Delta x/D = 0.007$, $\Delta y/D = 0.007$ and $\Delta z/D = 2\pi\times0.007/48$ where $D$ is the base diameter.

The time step size is determined by the CFL (Courant-Friedrichs-Lewy) condition [8] which is given by,

$$\Delta t = \min \frac{ChJ^*}{|U^*| + |V^*| + |W^*| + c\left(\sqrt{\xi_x^{*2} + \xi_y^{*2} + \xi_z^{*2}} + \sqrt{\eta_x^{*2} + \eta_y^{*2} + \eta_z^{*2}} + \sqrt{\zeta_x^{*2} + \zeta_y^{*2} + \zeta_z^{*2}}\right)}, \tag{14}$$

with,

$$U^* \equiv \xi_x^* u + \xi_y^* v + \xi_z^* w, \quad V^* \equiv \eta_x^* u + \eta_y^* v + \eta_z^* w, \quad W^* \equiv \zeta_x^* u + \zeta_y^* v + \zeta_z^* w$$

where the Courant number C = 1.0 is used in the present computation and $c$ is the local speed of sound. In the evaluation of the time step, the operator 'min' in Eq. (14) does not include the centerline as the denominator approaches infinity there and the Euler equations are not solved on the centerline as remarked in the previous sections.

A steady-state flow field is first acquired by solving the two-dimensional axisymmetric Euler equations. This is used as the initial condition for the present three-dimensional computation. Figure 3(a) shows the pressure contours and Fig. 3(b) shows the Mach number contours. There is a recirculation bubble in cone base region. Calvert [1] deduced this characteristic form from his experimental measurements. The calculation, using the OpenMP [9] parallel libraries, is performed on an IBM SP2 parallel computer at the Pennsylvania State University Center for Academic Computing [10]. Occupying four CPUs, the actual computation time is 4.45 seconds/iteration, which gives 7 microseconds/iteration/number of grid points. The computation performs 500,000 iterations before a fully developed wake flow is generated.

### B. Initial Triggering of Vortex Shedding

In the early stages of the computation, it is difficult and time-consuming to initiate vortex shedding in the inviscid flow without some excitation. To start the first vortex shedding, the velocity normal to the base of the cone is excited in the form

$$u_w(r,\theta,t) = \varepsilon u_\infty \sin^2\left(\frac{\pi r}{R}\right)\cos(2\theta)\exp\left[-(\ln 2)(f_s t)^2\right]\sin(2\pi f_s t), \quad (0 \le r \le R,\ 0 \le \theta < 2\pi) \tag{15}$$

where $\varepsilon$ is the amplitude of the fluctuation, $u_\infty$ is the free-stream velocity, $r$ is the radial distance, $R$ is the base radius, $\theta$ is the azimuthal angle, and $f_s$ is the frequency of the excitation. In Eq. (15), the distribution of the excitation velocity has four lobes with alternating signs on the cone base, and the amplitude decreases rapidly to half its initial value in one time period. In the present computation, the initial amplitude is chosen as $\varepsilon$ = 0.05 and the frequency is $f_s$ = 0.171 $u_\infty/D$. This corresponds to the regular vortex shedding frequency or the Strouhal number observed by Calvert [1]. Soon after the excitation vanishes, a non-axisymmetric flow field develops and the first vortex shedding occurs.

### C. Investigation of Flow Field

The unsteady wake flow may be visualized by the instantaneous pressure and Mach number contours shown in Figs. 4 and 5 at the final time step (non-dimensional time is $t^* = u_\infty t/D$ = 64.04). Figure 4 shows the longitudinal distribution in a side view, and Fig. 5 shows the circumferential distribution in a rear view. The instantaneous three-dimensional unsteady flow field is very different from the two-dimensional axisymmetric steady flow field shown in Fig. 2. The pressure contours show many irregular vortices generated from the edge of the cone base and the Mach number contours show strong flow fluctuations behind the cone base. The flow pattern appears to be random or chaotic unlike the regular Kármán vortex street [11] behind a two-dimensional bluff body. It can be seen that some vortices pair and merge mutually in the downstream region. This results in a large-scale motion of the far wake. However, the vortices very near the outflow boundary are dissipated non-physically because of the lack of grid resolution.

In order to investigate the unsteady motion of the wake structure, time-traced snapshots of vorticity magnitude iso-surfaces are presented in Fig. 6. Figure 6 shows some vortex rings near

the cone base that have non-axisymmetric distorted shapes, which seems to induce the chaotic flow fluctuations in the near wake and the spontaneous vortex shedding downstream. It is also shown that the vortex rings in the near wake region interact each other and change their shapes into the axial vortex tubes in some transitional region away from the cone base at a distance nearly equal to the wall diameter ($x/D \approx 1$). Further downstream, the vortex tubes shed from the transitional region possess a velocity component in the circumferential direction. This results in a spiral motion of the far wake structure. Moreover, the vortex tubes sometimes twist, bend and stretch in the far wake region. These phenomena occur quite randomly and it is almost impossible to pick up any two snapshots with the same instantaneous flow field during the entire computation. It is difficult to discern any periodicity from these time-traced observations of the flow field. In the next subsection, a frequency analysis of the flow signals is presented to quantify the periodicity.

### D. Analysis of Flow Signals

The unsteady pressure and axial velocity along the centerline behind the cone are obtained as a function of time in the fully developed wake stage. By averaging the signals in time, the axial variations of the mean pressure and axial velocity may be obtained. They are compared with Calvert's experimental data [1] in Figs. 7 and 8. Figure 7 shows that the mean pressure coefficient from the present computation agrees with the experimental data well in the near wake region up to the location of its minimum value. It then recovers faster to the free-stream value with a smaller overshoot than the experimental data in the far wake region. Figure 8 shows that the mean velocity curve of the present computation is a little more positive than the experimental data and recovers slightly faster to the free-stream value too. The agreement between the predicted pressure coefficient and mean axial velocity is much better than that achieved in the low-order, unstructured grid calculations of Long *et al.* [2]. The mean stagnation point, where

$\overline{u} = 0$ and $\overline{C_p} = 0$, of the present computation is slightly closer to the cone base than that of the experiment. It is likely that the small discrepancy between the present results and the experiment data is caused by the difference between the inviscid flow and the real viscous flow. The Euler equations have no physical viscosity that dissipates out the flow kinetic energy as the wakes move downstream, and the inviscid flow passes over a relatively smaller body in its effective size than the real viscous flow since there is no boundary layer displacement effect.

Two variables are defined in Ref. 1 to characterize the fluctuating components of the flow. They are denoted by,

$$\theta \equiv \frac{\overline{u'^2}^{1/2}}{u_\infty} \times 100 \quad \text{and} \quad \phi \equiv \frac{\overline{u'^2}^{1/2}}{\overline{u}_m} \times 100$$

where $u' = u_m - \overline{u}_m$ is the fluctuation of the axial velocity about its mean value and $u_m = |u|$ is the magnitude of the axial velocity. Thus, $\theta$ is a measure of the absolute level of the velocity fluctuations and $\phi$ represents the local turbulence intensity. The axial variations of $\theta$ and $\phi$ are shown and compared with the experimental data in Figs. 9 and 10, respectively. Figure 9 shows that the present results agree well overall with the experimental data except for a slight overshoot in the near wake region and a small underprediction in the far wake region. Figure 10 shows the same kind of discrepancy between the present results and the experimental data in terms of the shortening of the axial development as is explained for the mean flow results in Figs. 7 and 8 above. The predicted overall amplitude of the fluctuations agrees very well with the measurements. It is much better than the predictions by Long *et al.* [2] particularly in the far wake region. However, the present grid is much finer in that region and the order of accuracy of the present numerical scheme is higher. A comparison of Figs. 8 and 10 shows that the region of the highest local turbulence intensities is in the vicinity of the stagnation point. This is consistent with Calvert's [1] observations. However, this high value is associated with the lower mean

velocity at this location rather than an increase in the absolute value of the velocity fluctuations. In fact, as seen in Fig. 9, there is a slight decrease in the absolute value of the fluctuations in this region.

The point of the mean pressure minimum in Fig. 7 corresponds to the transitional region ($x/D \approx 1$) where the axial vortex tubes start to form as described in the previous subsection. It coincides with the point of the mean velocity minimum where the highest speed of reversed flow on the centerline occurs as shown in Fig. 8. This point has significance in estimating the starting position of the periodic vortex shedding. Calvert [1] remarked that a periodic wake motion first appears in the region of the mean pressure minimum and the periodicity presumably arises from the instability of the free shear layer in an adverse pressure gradient. He also mentioned that the periodicity is most prominent in the region of the mean pressure maximum. In order to quantify the periodicity, the frequency spectrum of the axial velocity is obtained at the point of the mean pressure maximum ($x/D$ = 2.0). This is shown in Fig. 11. The highest peak in Fig. 11 shows that there is a strong periodic wake motion at a non-dimensional frequency of $fD/u_\infty$ = 0.171. This is exactly the Strouhal number found by Calvert [1]. The existence of this peak is taken as further evidence that the present computation succeeds in simulating the vortex shedding process accurately.

## V. Conclusions

The subsonic inviscid wake flow past a cone has been simulated using high-order finite difference schemes on structured grids. The present computation, performed in an axisymmetric structured grid system is achieved by changing the form of the flux vectors in the Euler equations to remove the centerline singularity in the generalized coordinates. This approach makes it possible to investigate the complex wake flow field and to obtain the accurate values of the flow properties. It is shown that the vortex rings in the near wake change their shapes into axial

vortex tubes in the far wake through a transitional region where periodic vortex shedding begins. A spiral motion of the wake is found. The mean flow pattern agrees well with the experimental data when account is taken of the likely differences between the inviscid and the viscous cases. It is confirmed that the point of the mean pressure minimum is the starting position of the periodic vortex shedding. A spectral analysis of this periodic phenomenon shows that the Strouhal number is 0.171. This is in exact agreement with the experimental observation. On the basis of the very good agreement between the predictions and experiment, it is expected that the present methodology may be used for further analysis of wake-dominated flows past an axisymmetric blunt-based body.

## Acknowledgment

This research was supported by NASA Langley Research Center under Grant NRA 98-LaRC-5. The authors would like to acknowledge Center for Academic Computing at The Pennsylvania State University for providing the supercomputer resources.

## References

1. Calvert, J. R., "Experiments on the Low-Speed Flow past Cones," *Journal of Fluid Mechanics*, Vol. 27, part 2, 1967, pp. 273-289.
2. Long, L. N., Souliez, F., and Sharma, A., "Aerodynamic Noise Prediction Using Parallel Methods on Unstructured Grids," AIAA Paper 2001-2196, May 2001.
3. Kim, J. W., and Lee, D. J., "Optimized Compact Finite Difference Schemes with Maximum Resolution," *AIAA Journal*, Vol. 34, No. 5, 1996, pp. 887-893.
4. Kim, J. W., and Lee, D. J., "Implementation of Boundary Conditions for Optimized High-Order Compact Schemes," *Journal of Computational Acoustics*, Vol. 5, No. 2, 1997, pp. 177-191.

5. Lockard, D. P., and Morris, P. J., "Radiated Noise from Airfoils in Realistic Mean Flows," *AIAA Journal*, Vol. 36, No. 6, 1998, pp. 907-914.

6. Kim, J. W., and Lee, D. J., "Adaptive Nonlinear Artificial Dissipation Model for Computational Aeroacoustics," *AIAA Journal*, Vol. 39, No. 5, 2001, pp. 810-818.

7. Kim, J. W., and Lee, D. J., "Generalized Characteristic Boundary Conditions for Computational Aeroacoustics," *AIAA Journal*, Vol. 38, No. 11, 2000, pp. 2040-2049.

8. Hirsch, C., "The Von Neumann Method for Stability Analysis," *Numerical Computation of Internal and External Flows*, 1st ed., Vol. 1, John Wiley & Sons, New York, 1992, pp. 283-341.

9. http://www.openmp.org

10. http://natasha.cac.psu.edu/beatnic/SPinfo/SP_features.php

11. Schlichting, H., "Outline of Boundary-Layer Theory," *Boundary Layer Theory*, 7th Ed., McGraw-Hill, New York, 1979, pp. 24-46.

## Table Caption

Table 1. List of optimized coefficients for compact finite difference schemes

## Figure Captions

Fig. 1. Diagram of computational domain

Fig. 2. Grid mesh system: (a) entire view, and (b) zoomed view

Fig. 3. Zoomed side view of axisymmetric steady-state flow field for the initial condition: (a) pressure ($p/p_\infty$), and (b) Mach number contours

Fig. 4. Zoomed side view of instantaneous flow field at the final time step: (a) pressure ($p/p_\infty$), and (b) Mach number contours

Fig. 5. Zoomed rear view of instantaneous flow field at the final time step ($x/D$ = 1.0 from the

cone base): (a) pressure ($p/p_\infty$), and (b) Mach number contours

Fig. 6. Time-traced snapshots of vorticity magnitude iso-surfaces (17 levels of $|\vec{\omega}|D/u_\infty$ from 0.0 to 0.002) in the interval of time $t_{n+1} - t_n = 0.642\, D/u_\infty$ between two successive pictures

Fig. 7. Axial variation of mean pressure along the centerline behind the cone

Fig. 8. Axial variation of mean axial velocity along the centerline behind the cone

Fig. 9. Axial variation of velocity fluctuations in terms of free-stream velocity

Fig. 10. Axial variation of velocity fluctuations in terms of the local axial velocity

Fig. 11. Spectrum of axial velocity fluctuations at the point of mean pressure maximum

| Equation (8) | Equation (9) | Equation (10) | Equation (11) |
|---|---|---|---|
| $a_1$ = 0.6511278808920836 | $a_{0,1}$ = -3.061503488555582 | $a_{1,0}$ = -0.5401943305881343 | $a_{2,0}$ = -0.1327404414078232 |
| $a_2$ = 0.2487500014377899 | $a_{0,2}$ = 5.917946021057852 | $a_{1,2}$ = 0.8952361063034303 | $a_{2,1}$ = -0.6819452549637237 |
| $a_3$ = 0.006144796612699781 | $a_{0,3}$ = 0.4176795271056629 | $a_{1,3}$ = 0.2553815577627246 | $a_{2,3}$ = 0.7109139355526556 |
| $\alpha$ = 0.5775233202590945 | $\alpha_{0,1}$ = 5.870156099940824 | $a_{1,4}$ = 0.007549029394582539 | $a_{2,4}$ = 0.2459462758541114 |
| $\beta$ = 0.08953895334666784 | $\beta_{0,2}$ = 3.157271034936285 | $\alpha_{1,0}$ = 0.1663921564068434 | $a_{2,5}$ = 0.003965415751510620 |
| | | $\alpha_{1,2}$ = 0.7162501763222718 | $\beta_{2,0}$ = 0.03447751898726934 |
| | | $\beta_{1,3}$ = 0.08619830787164529 | $\alpha_{2,1}$ = 0.4406854601950040 |
| | | | $\alpha_{2,3}$ = 0.6055509079866320 |
| | | | $\beta_{2,4}$ = 0.08141498512587530 |

Table 1

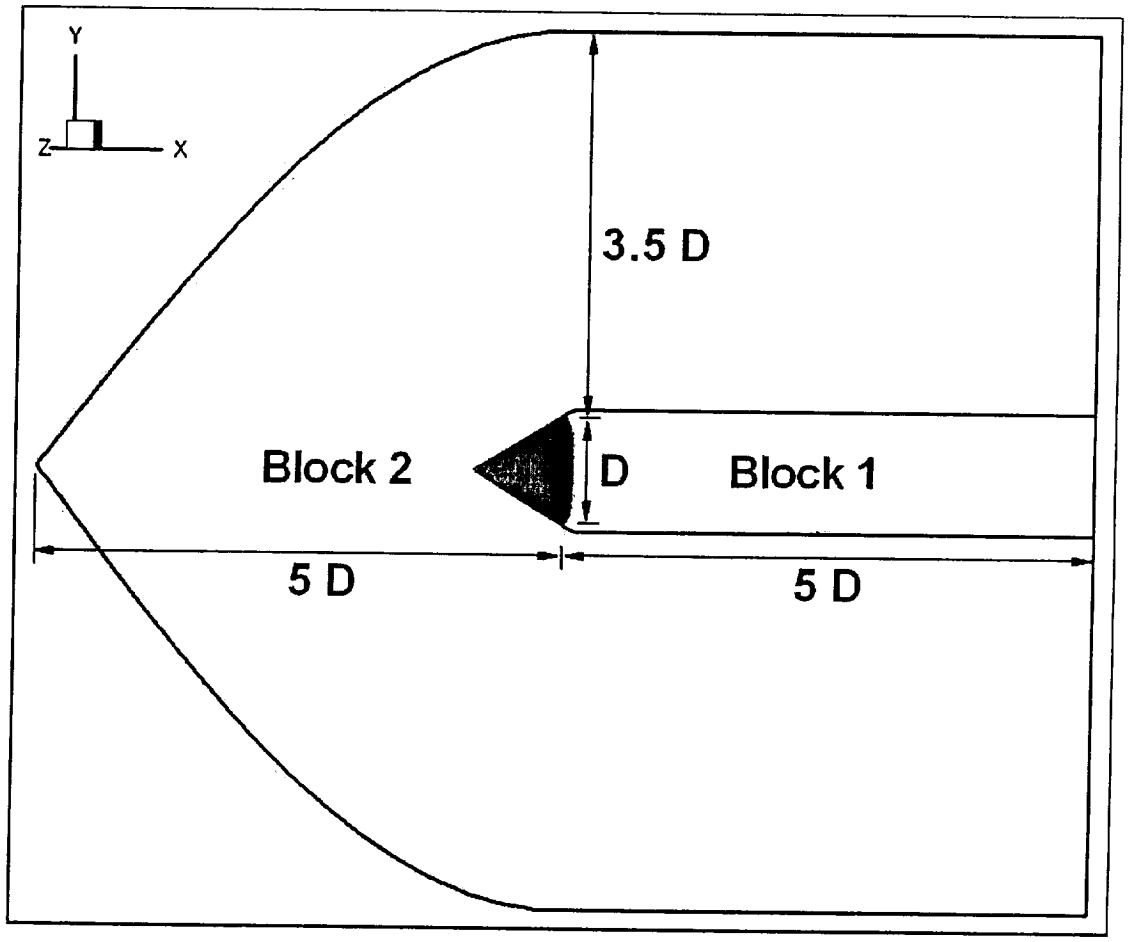


Figure 1

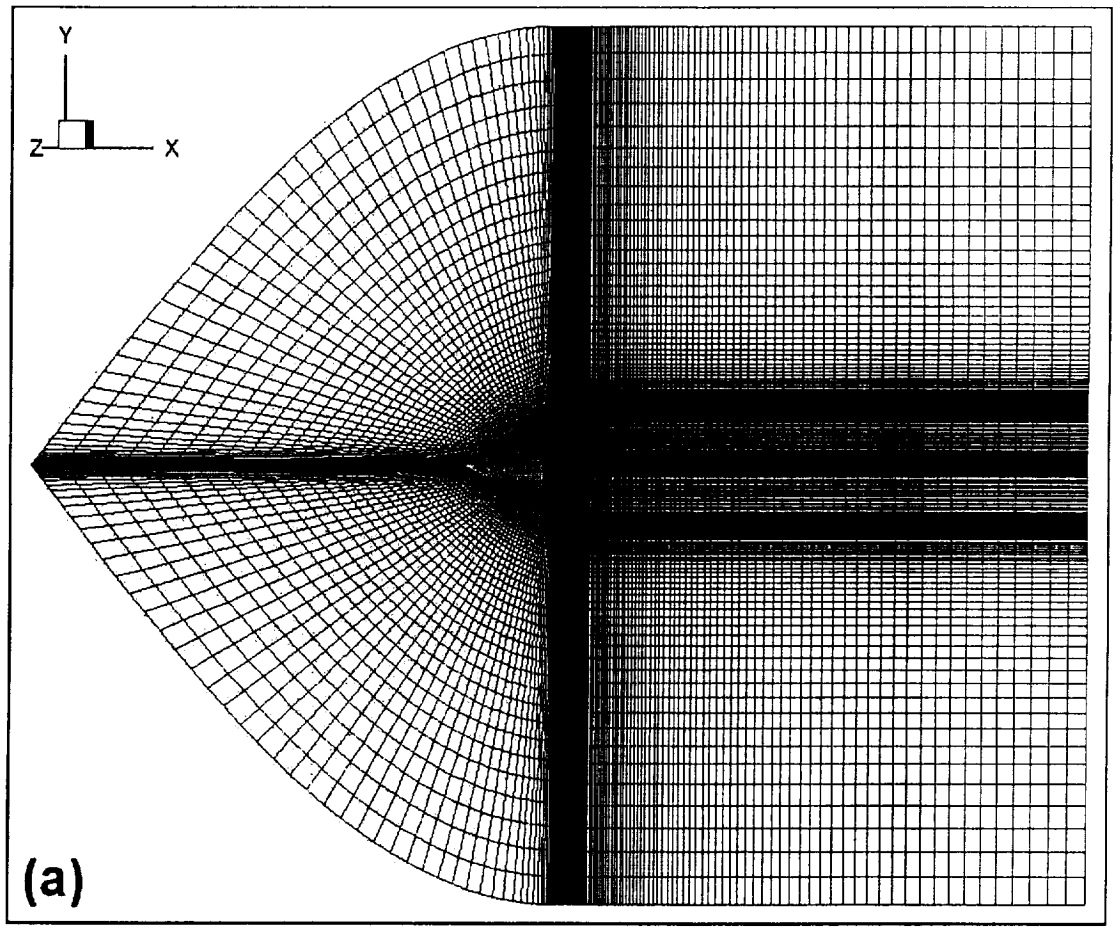


Figure 2-(a)

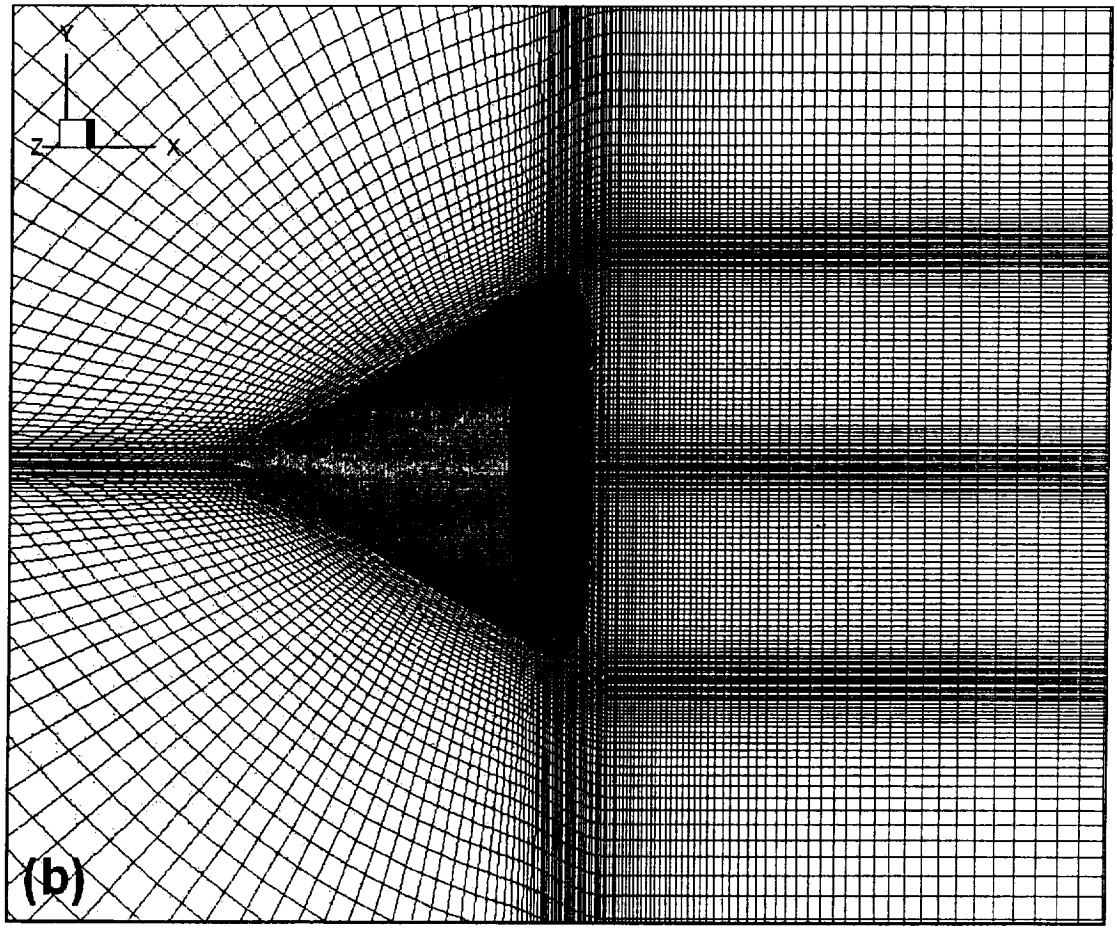


Figure 2-(b)

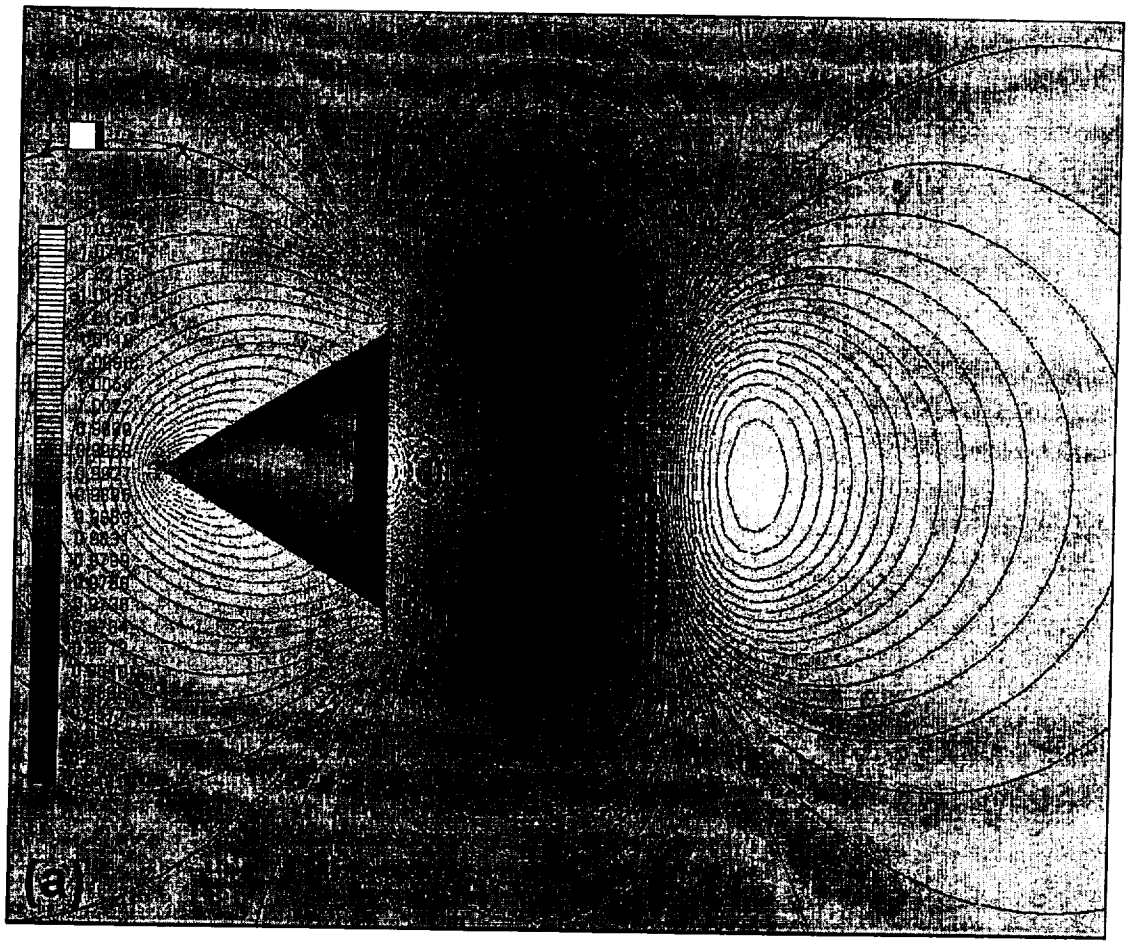


Figure 3-(a)

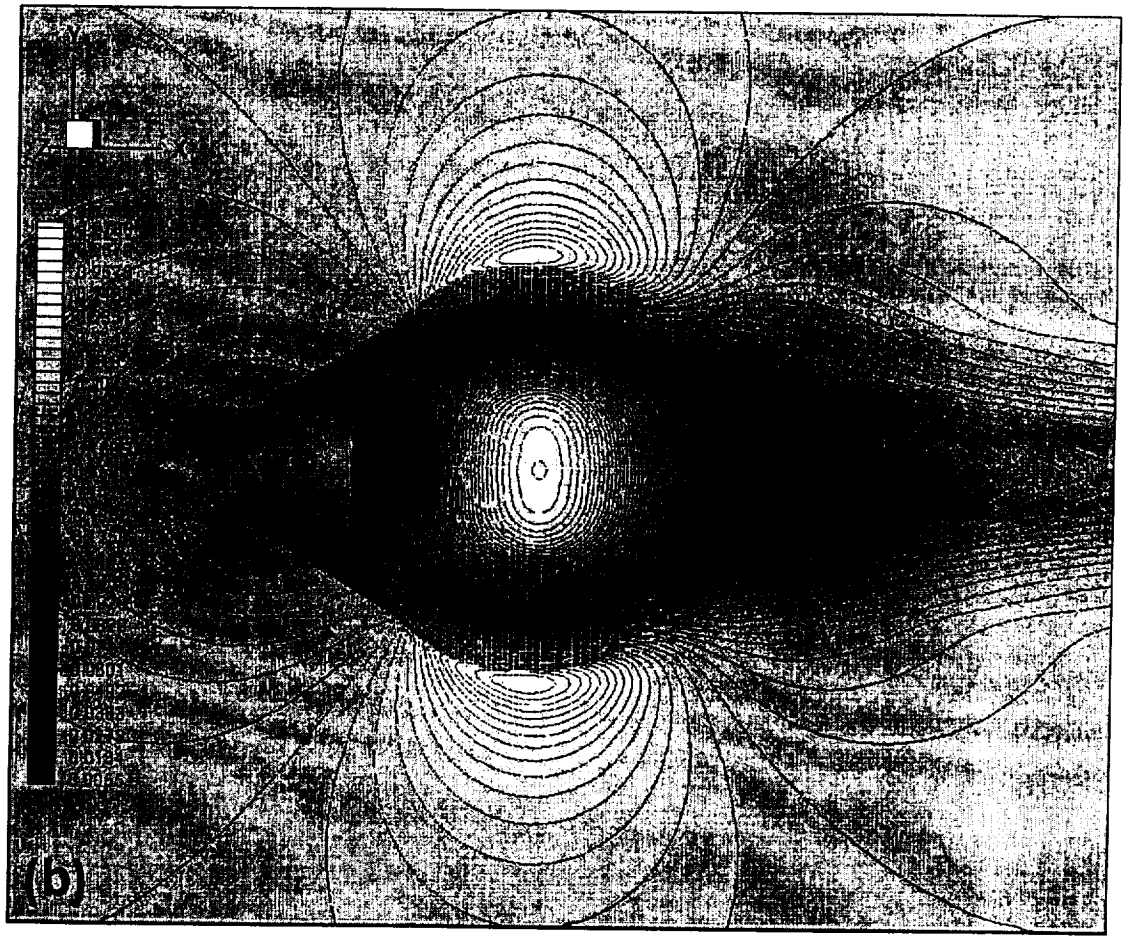


Figure 3-(b)

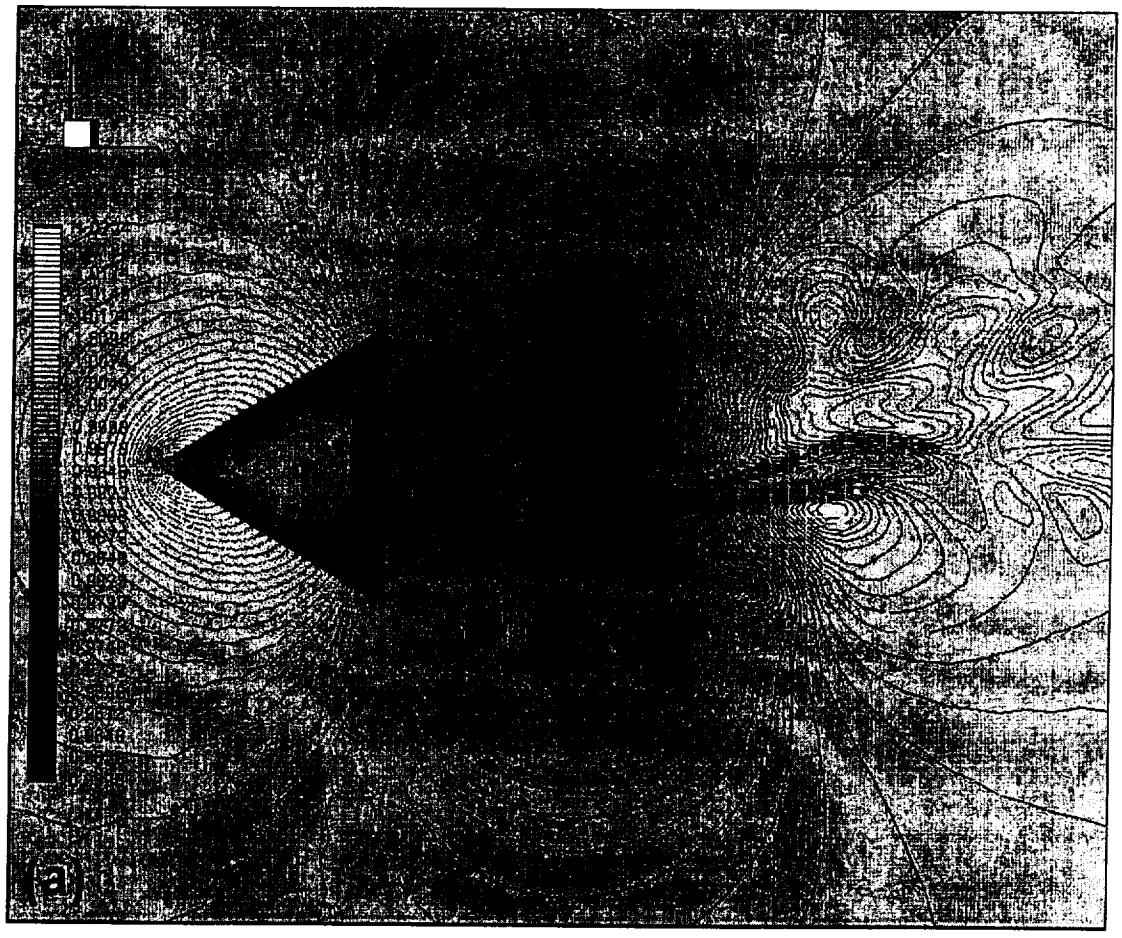


Figure 4-(a)

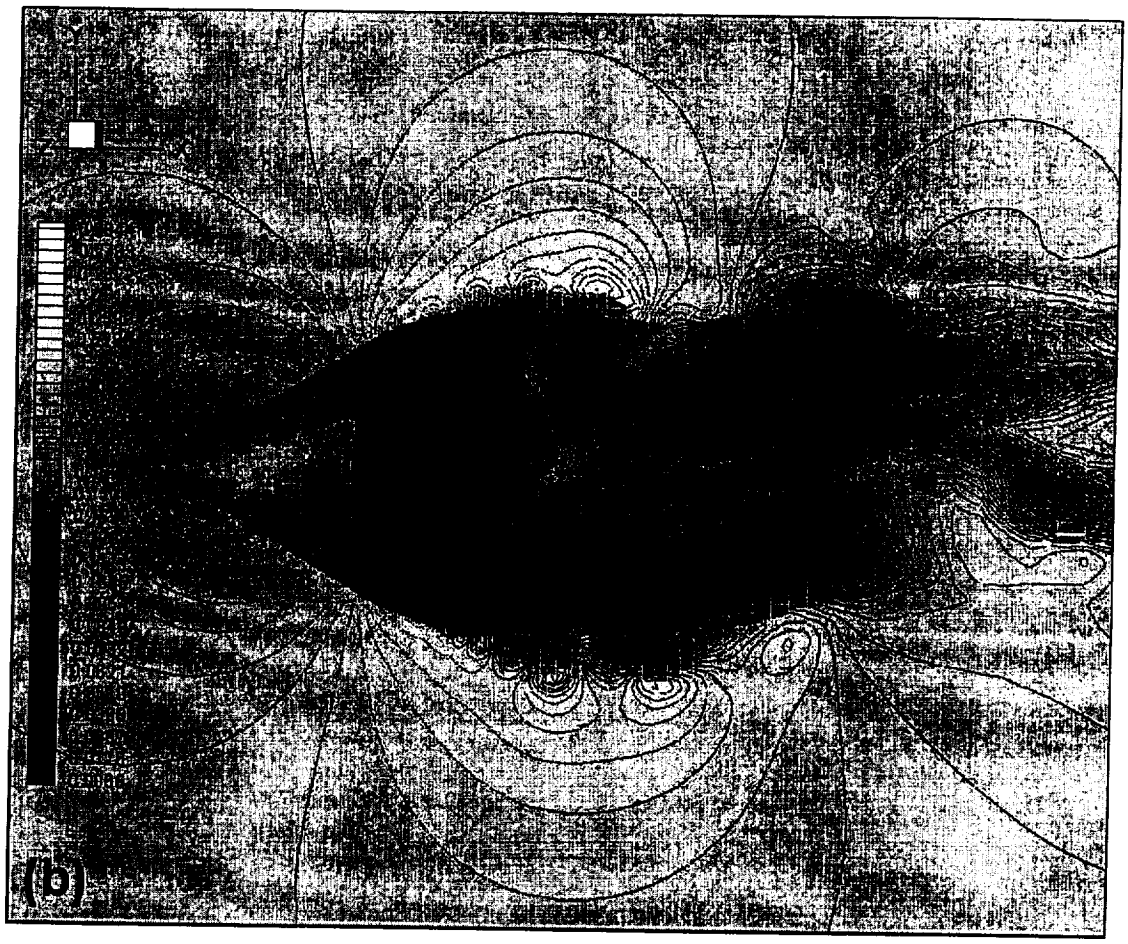


Figure 4-(b)

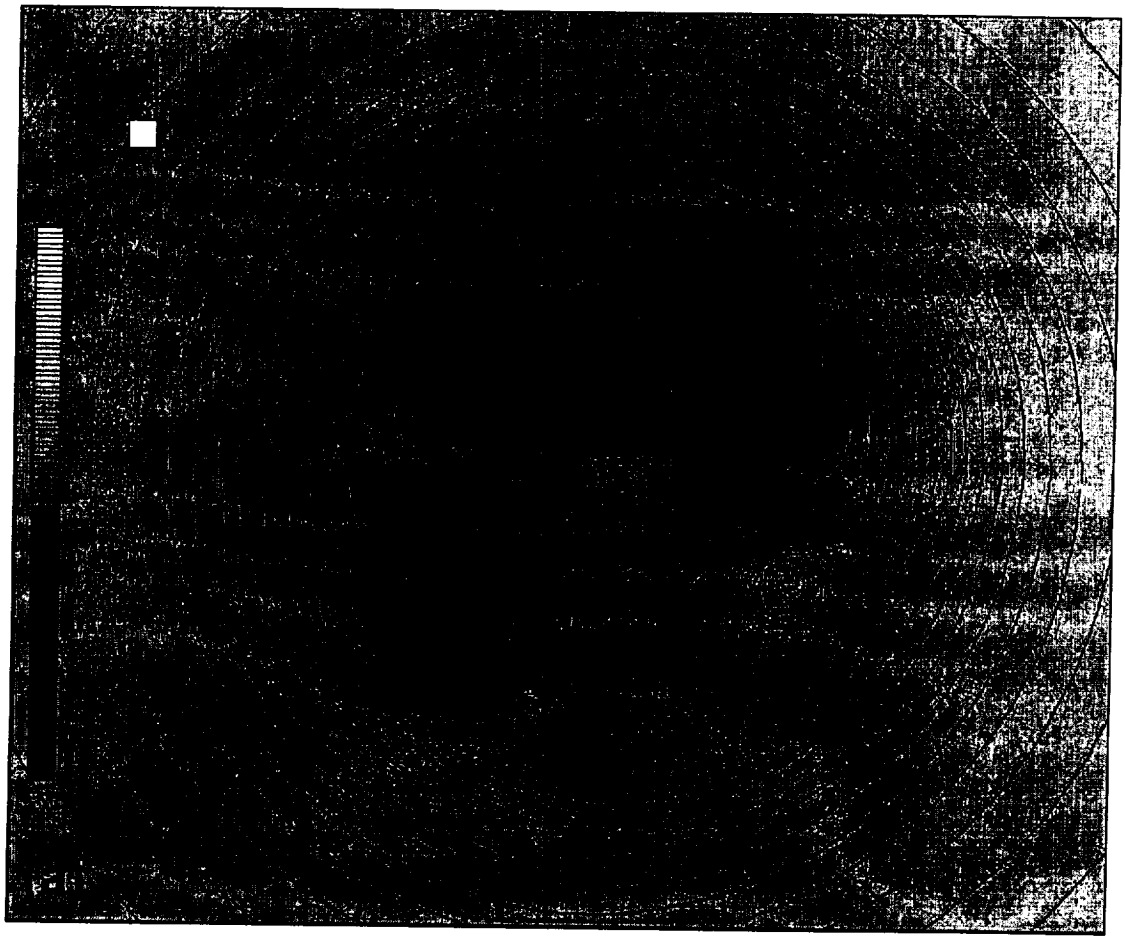

Figure 5-(a)

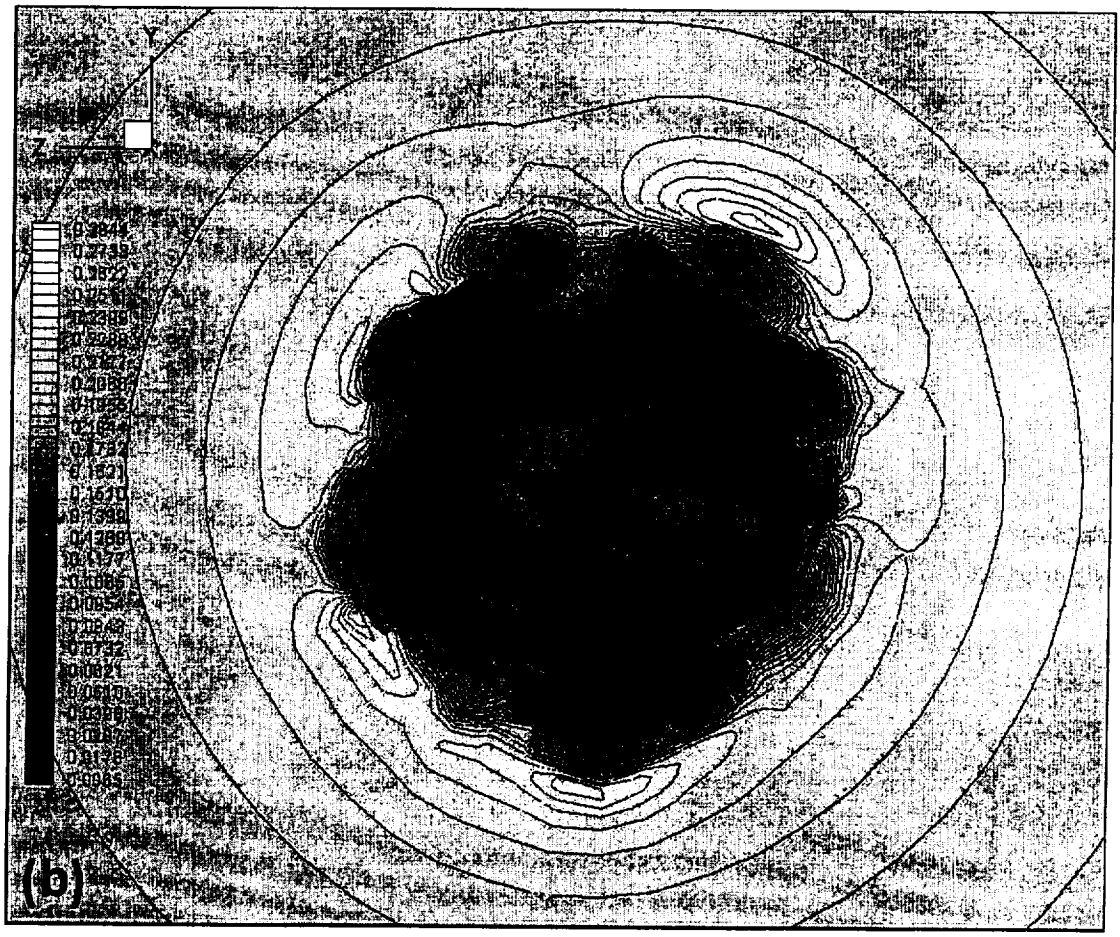


Figure 5-(b)

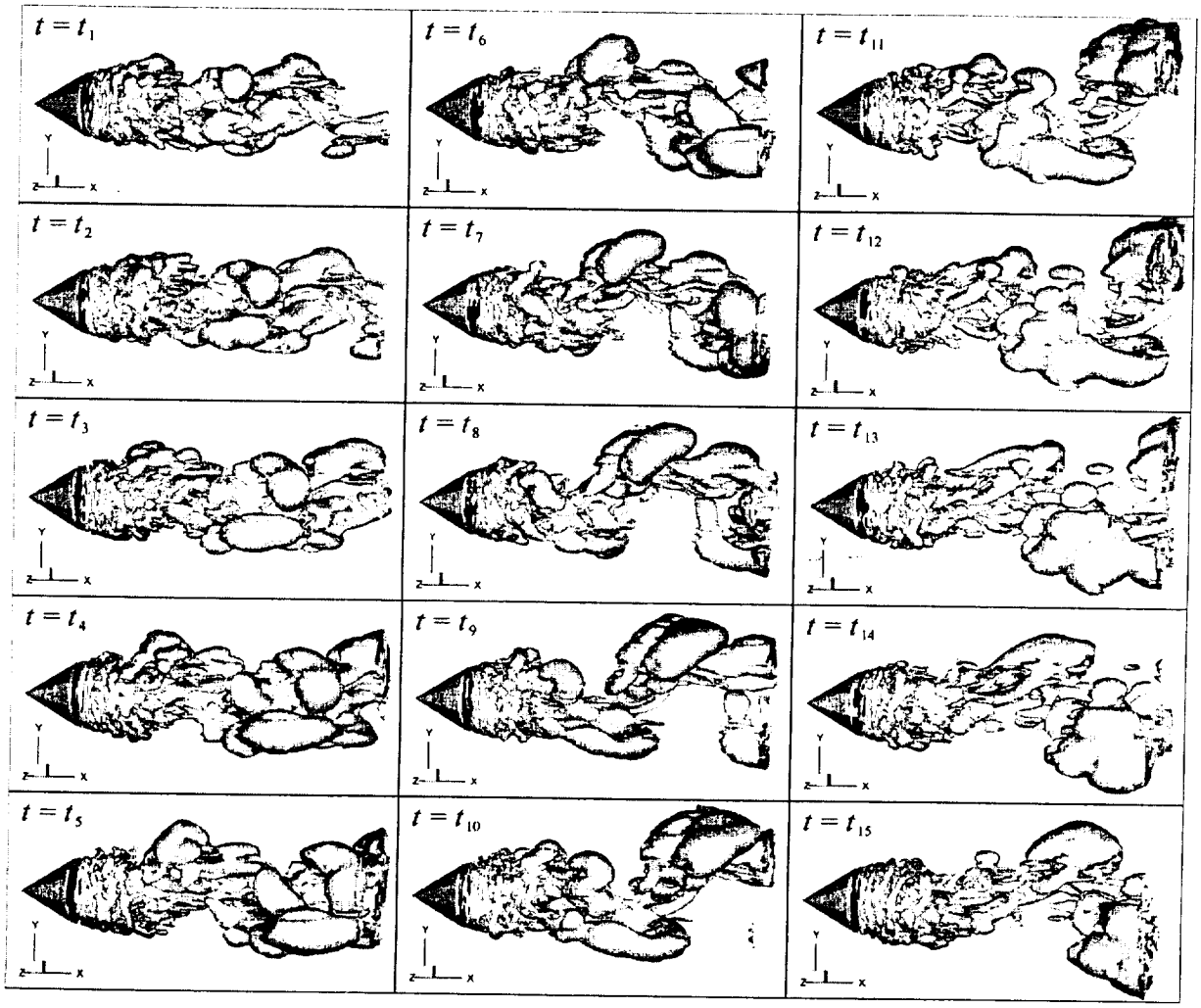
$t = t_1$
$t = t_6$
$t = t_{11}$
$t = t_2$
$t = t_7$
$t = t_{12}$
$t = t_3$
$t = t_8$
$t = t_{13}$
$t = t_4$
$t = t_9$
$t = t_{14}$
$t = t_5$
$t = t_{10}$
$t = t_{15}$

Figure 6

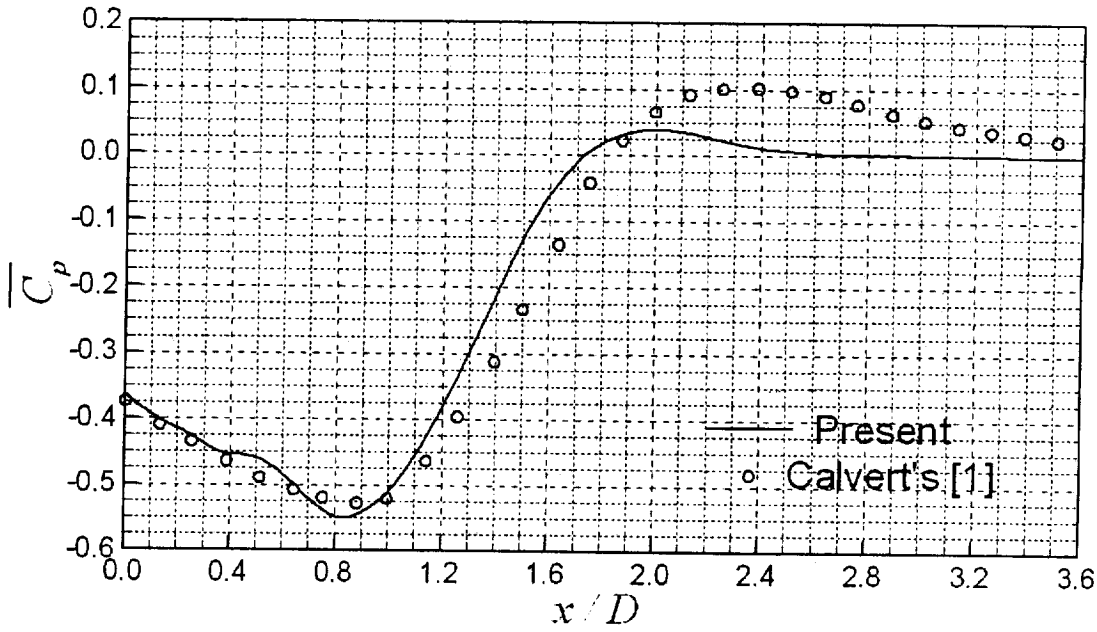
0.2
0.1
0.0
-0.1
-0.2
-0.3
-0.4
-0.5
-0.6
$\overline{C_p}$
0.0
0.4
0.8
1.2
1.6
2.0
2.4
2.8
3.2
3.6
$x/D$
Present
Calvert's [1]

Figure 7

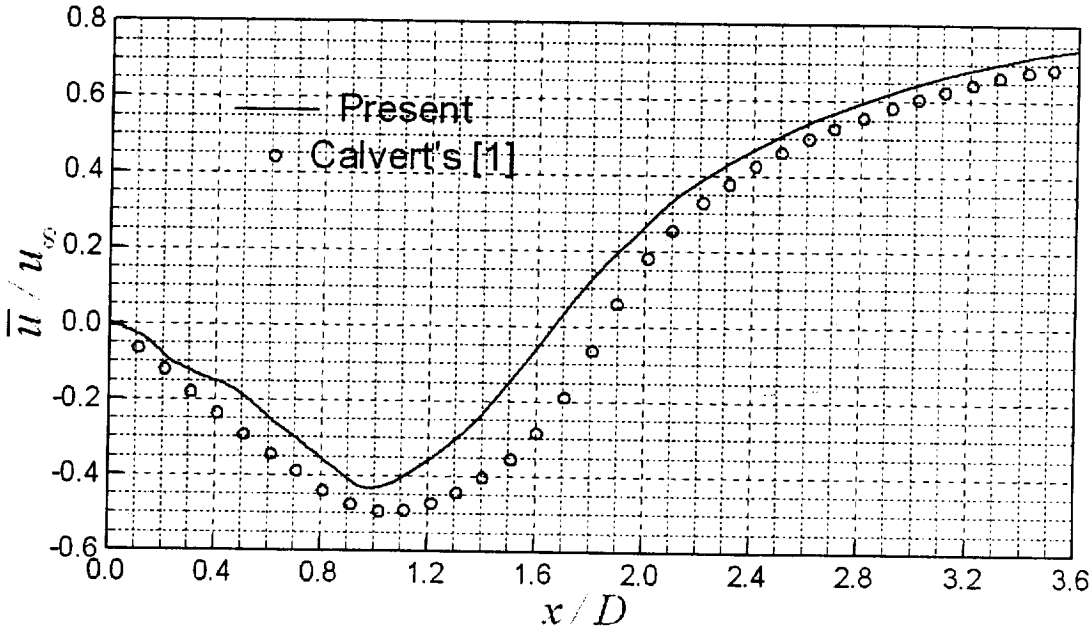
Present
Calvert's [1]
$\overline{u} / u_\infty$
$x / D$
0.8
0.6
0.4
0.2
0.0
-0.2
-0.4
-0.6
0.0
0.4
0.8
1.2
1.6
2.0
2.4
2.8
3.2
3.6

Figure 8

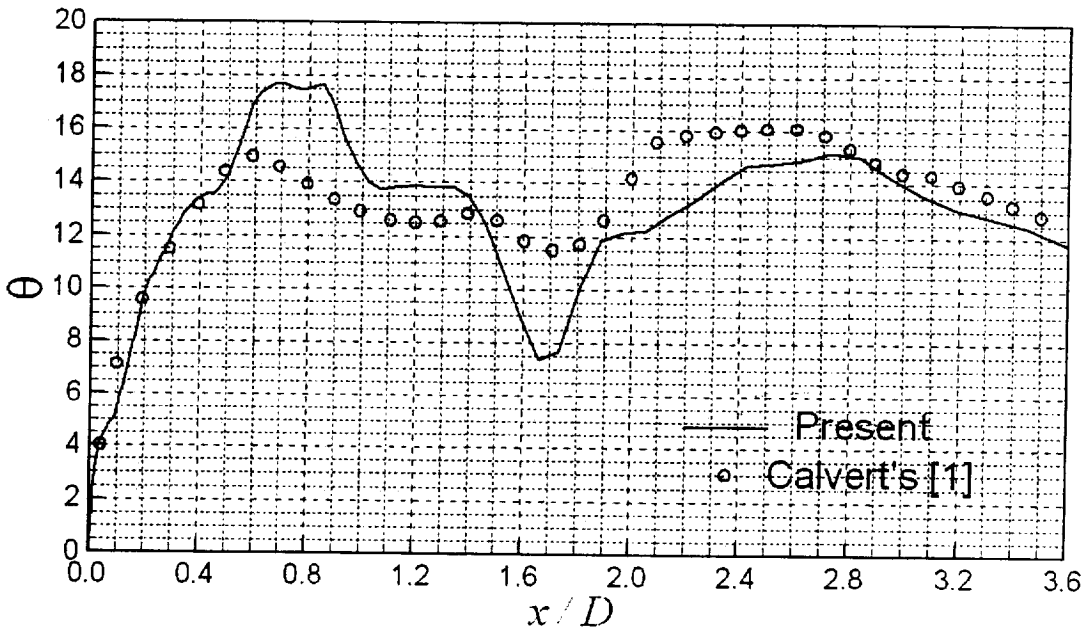
20
18
16
14
12
10
8
6
4
2
0
θ
0.0
0.4
0.8
1.2
1.6
2.0
2.4
2.8
3.2
3.6
x / D
Present
Calvert's [1]

Figure 9

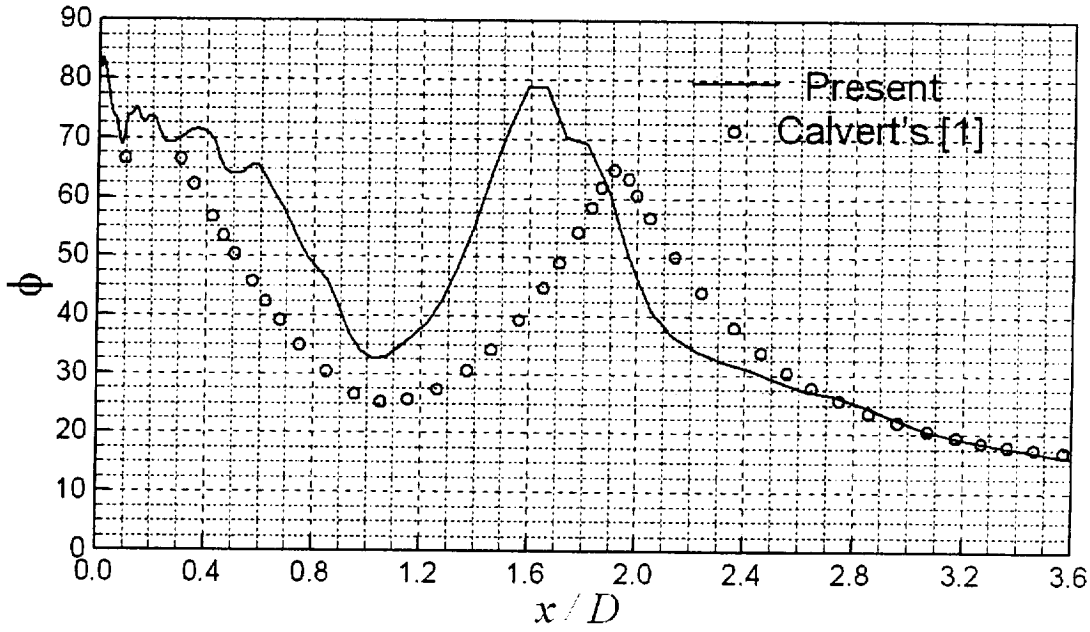
90
80
70
60
50
40
30
20
10
0
ϕ
0.0
0.4
0.8
1.2
1.6
2.0
2.4
2.8
3.2
3.6
x / D
Present
Calvert's [1]

Figure 10

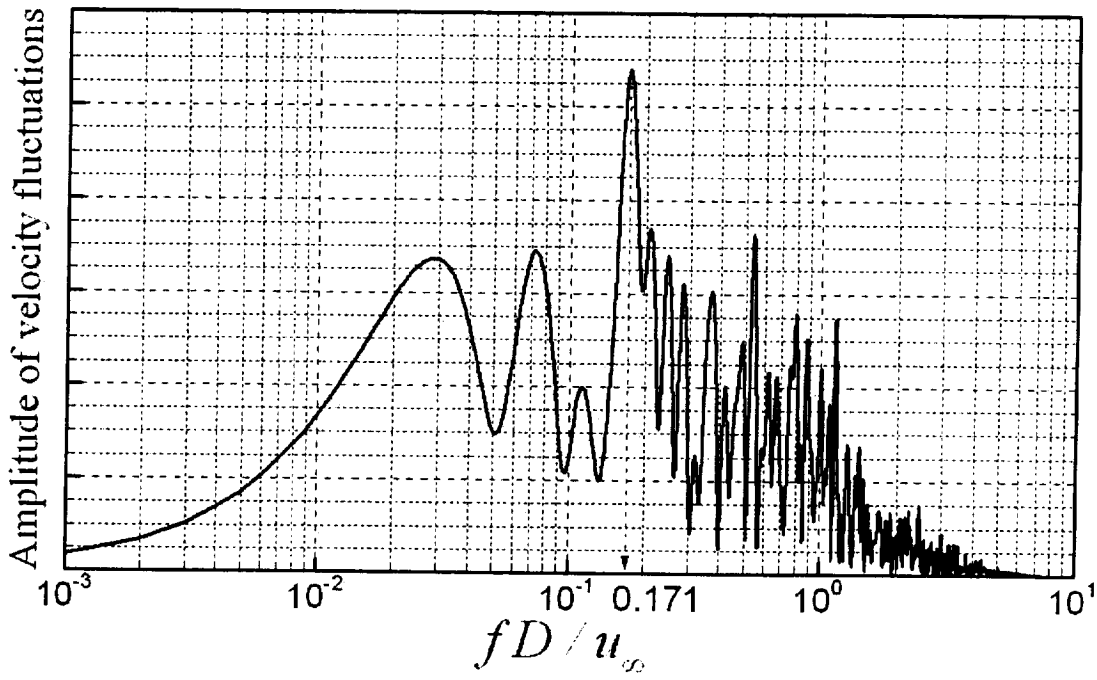
Amplitude of velocity fluctuations
10-3
10-2
10-1
0.171
100
101
f D / u∞

Figure 11

# The Discontinuous Galerkin Finite Element Method A Brief Review of the Method and its Applications in Aeroacoustics

Preetham Rao*
*Department of Aerospace Engineering*
*The Pennsylvania State University*
*University Park, PA 16802, U.S.A.*

**Abstract**

The preliminary implementation and testing of the quadrature free Discontinuous Galerkin Finite Element Method in one and two dimensions are discussed. With an objective of understanding the method, algorithms to solve the linear scalar advection equation with periodic boundary conditions using the method have been written and executed successfully. A qualitative comparison of Lagrange polynomials and simple monomials as choices for the basis function set is made. Results from the algorithms using both Lagrange Polynomials and simple monomials as basis functions are also presented.

## 1 Introduction to the Discontinuous Galerkin Method

Convection dominated problems arise in applications as diverse as aeroacoustics, gas dynamics, meteorology, oceanography, turbulent flows, viscoelastic flows, magneto hydrodynamics and electromagnetism, among many others. Devising robust, accurate, and efficient numerical methods for solving these problems is not a trivial task for two reasons. The first is that the exact solution of nonlinear problems develop discontinuities after finite time, and the second is that these numerical methods might display complicated and erroneous solutions at these discontinuities. Thus, while developing these numerical methods, care must be taken to guarantee that the discontinuities of the approximate solutions are physically relevant, and that the appearance of discontinuities in the approximate solution does not induce spurious oscillations [1].

The Discontinuous Galerkin Finite Element Method (DG method) is one of those methods that are being developed to successfully address the issues mentioned above. The original DG method was developed in 1973, but it is only recently that enhancement and evolution of the method are taking place. The method has been proven to be well suited for high order accurate large time scale simulations. An important distinction between the DG method and the conventional finite element methods is that

*Graduate Research Assistant

the resulting formulation is local to the element and the solution is not reconstructed by looking at the neighboring elements. Thus each element in the DG method can be thought of as an independent entity, merely requiring the boundary data from the surrounding elements. Since the DG method incorporates numerical fluxes and discontinuous elements, it can be considered as a generalization of finite volume methods. Owing to its unique finite element nature, the DG method has numerous advantages over classical finite volume and finite element methods such as [1, 2]:

- The DG method can be used to obtain uniformly high order accurate solutions.
- The method is highly parallelizable since the elements are discontinuous and the mass matrix is block diagonal and readily invertible.
- It is suited for complex geometries since it can be used on unstructured grids. The method has also been shown to be immune to mesh discontinuities. It also requires simple treatment of the boundary conditions.
- It can easily handle adaptive strategies, since refining or coarsening the grid can be achieved without considering the continuity restrictions typical to the conforming elements.
- It has several useful mathematical properties with regards to stability and convergence.
- The method is compact, since each element is independent. This compactness allows for a structured and simplified coding for the method.
- The method allows for heterogeneity in the elements, that is, the order of accuracy, shape, and even the choice of governing equations can vary from element to element.

Although the DG method is less susceptible to the problems that are common in finite difference schemes, it is not without a few weaknesses [2]. The method has been recognized as expensive, in terms of both computational operation count and storage requirements. Although theoretically the method can be applied to an element of any shape, the requirement of numerical quadrature for the integrals in the formulation has restricted the applications to hexahedral and quadrilateral elements. The recently developed [3] quadrature free DG method tries to resolve these problems by using polynomial basis functions, the product of which can be integrated without numerical quadrature.

The rest of this report deals with the quadrature free DG method applied to the scalar advection equation, with periodic boundary conditions. Results for one-dimensional linear and a nonlinear advection equation are presented, followed by solutions of the two-dimensional linear advection equation on a square domain.

# 2 Formulation of the DG Method

Let the solution in an arbitrary domain be governed by a conservation equation of the form

$$u_t + \nabla \cdot \vec{F} = 0 \tag{1}$$

Let the domain be divided into smaller elements $\Omega(x, y, z)$ that span the domain. Let the solution in each element be approximated using an expansion of a basis set given by

$$u_\Omega = \sum_{j=1}^{N+1} b_j u_j \tag{2}$$

$$B \Rightarrow \{b_k, 1 \leq k \leq N(p,d) + 1\} \tag{3}$$

The number of basis functions $N+1$ depends on the order of expansion denoted by $p$, and the number of dimensions, $d$. Application of the traditional Galerkin method to equation (1) using (2) and (3) gives,

$$\int_\Omega b_k \Big(u_t + \nabla \cdot \vec{F}\Big) d\Omega = 0 \tag{4}$$

for $k = 1 \ldots N+1$.

Using (2) and integrating by parts, equation (4) can be recast as,

$$\int_\Omega b_k \sum_{j=1}^{N+1} b_j \left(\frac{\partial u_j}{\partial t}\right) d\Omega - \int_\Omega \nabla b_k \cdot \vec{F} d\Omega + \int_{s_\Omega} b_k \vec{F}_R d\vec{s} = 0 \tag{5}$$

for $k = 1 \ldots N+1$.

where $d\vec{s}$ is the normal surface area element (or the line element in 2D), and $\vec{F}_R$ is the Riemann flux vector through the surface element, which will be approximated using the flux values of the element and the neighboring element.

It is convenient to carry out the integrations in the formulation (5) in transformed coordinates. In a conventional finite element method using quadrature, the integrals are calculated on a mapped element (denoted by $\Delta$), but the final equation is evaluated and assembled in the real coordinates of $\Omega$. Since there is no assembling of the elements involved in the DG method, by mapping even the variables $u_j$ into the transformed coordinates, one can get a compact form of the equation (5). If the transformation from $\Omega$ to $\Delta$ is linear, the storage requirements will be minimized. This will be explained in detail below.

Let the coordinates in the transformed space be $\xi$, $\eta$ and $\zeta$. Let the unknown variables in the transformed element $\Delta(\xi, \eta, \zeta)$ be denoted as $v_j$. Then,

$$\int_\Delta b_k \sum_{j=1}^{N+1} b_j \left(\frac{\partial u_j}{\partial t}\right) |J| d\Delta - \int_\Delta J^{-1} \nabla b_k \cdot \vec{F} d\Delta + \int_{s_\Delta} b_k \vec{F}_R \cdot |J_s| d\vec{s} = 0 \tag{6}$$

for $k = 1 \ldots N+1$, where $J \equiv \frac{\partial(x,y,z)}{\partial(\xi,\eta,\zeta)}$, and $J_s$ is the Jacobian of the surface (or line) coordinate transformation.

In particular, considering a linear advection equation in 2D, the flux is given by

$$\vec{F}_\Omega = \hat{i} a_x u + \hat{j} b_y u \equiv \vec{F}_\Delta = \hat{i} a_x v + \hat{j} b_y v = \hat{i} a_x \sum_{j=1}^{N+1} b_j v_j + \hat{j} b_y \sum_{j=1}^{N+1} b_j v_j \tag{7}$$

and (6) can be written as,

$$M_{ij}\left(\frac{\partial v_j}{\partial t}\right) - K_{ij}v_j + \int_{s_\Delta} b_k \vec{F}_R \cdot |J_s| d\vec{s} = 0 \tag{8}$$

where

$$M_{ij} = \int_\Delta b_j b_k |J| d\Delta \tag{9}$$

and

$$K_{ij} = \int_\Delta J^{-1} \nabla b_k b_j |J| \Delta \tag{10}$$

for $k = 1 \ldots N+1, j = 1 \ldots N+1$.

Due to the presence of the term $J^{-1}$, the matrix $K_{ij}$ is made up of a sum of several matrices. The Riemann flux is approximated as a Lax-Friedrich's flux of the form

$$\vec{F}_R d\vec{s} = \frac{1}{2}\left\{\left(\vec{F}_l + \vec{F}_r\right)\cdot \vec{n} - \alpha\left(V_r - V_l\right)\right\} ds \tag{11}$$

where $\vec{F}_l$ is the flux of the element to the left of the edge, and $vecF_s$ is that of the element to the right of the edge. $\vec{n}$ is the unit normal to the edge from left to right, and $\alpha$ is a smooth positive function.

# 3 Computational Aspects of the DG Formulation

The number of operations and the amount of storage required for the calculation of the integrals in the above formulation are determined by:

1. the order of the coordinate transformation and
2. the choice of basis functions.

If the transformation is linear, then $J$ is a matrix made up of constants and $|J|$ is independent of $\xi$ or $\eta$ . This means that a single mass matrix $M_{ij}$ and component stiffness matrices $K_{ij}$ can be used for all the elements, thus minimizing the required storage. This is accomplished by using arbitrary triangles with straight edges for $\Omega$ and an equilateral triangle for $\Delta$, with the origin at its centroid. This is displayed in Fig. 1.

$$\left\{ \begin{array}{c} x - x_0 \\ y - y_0 \end{array} \right\} = J_T \left\{ \begin{array}{c} \xi \\ \eta \end{array} \right\}, J_T = \left[ \begin{array}{cc} a1 & a2 \\ b1 & b2 \end{array} \right]$$

where

$$a1 = x_3 - x_2, a2 = 1/sqrt3(2x_1 - x_2 - x_3)$$

$$b1 = y_3 - y_2, b2 = 1/sqrt3(2y_1 - y_2 - y_3)$$

where $x_1 \ldots x_3$ and $y_1 \ldots y_3$ are as shown in the figure 1, and $x_0$ and $y_0$ are the coordinates of the centroid of the element $\Omega$. The transformation matrix $J_T$ will be

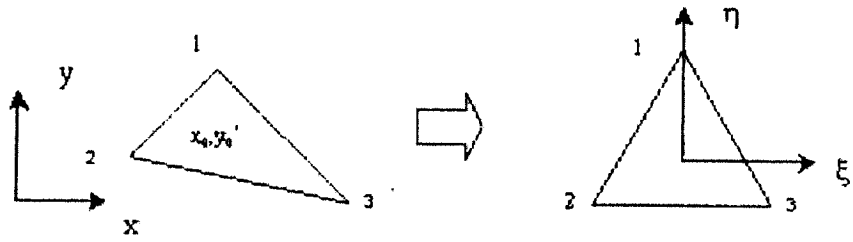


Figure 1: Sketch of the transformation from physical to canonical coordinates

different from, but related, to the transformation Jacobian $J$ which appears in Eqn. (8). ( $J_T = J'$ ).

This linear transformation also greatly reduces the computational time requirement. Since a single mass matrix is involved for all elements, it can be inverted prior to the main computation. Hence time marching for each element reduces from solving a system of equations to multiplying and adding matrices and vectors.

## 3.1 Choice of the basis functions

The choice of the expansion basis set greatly influences the computation time. Researchers [4] have worked on various polynomial basis function sets varying from simple monomials to orthogonal Legendre functions. A comparison of only the conventional Lagrange polynomials and simple monomials is presented here.

For a problem involving *nonlinear flux* , the integrals in $M_{ij}$ and $K_{ij}$ will involve products of more than two basis functions in their integrand. Choosing the conventional Lagrange polynomials for the basis set will necessitate excessive computation using numerical quadrature at each time step. Even if the integrals are computed analytically prior to the main computation, a huge storage will be required. The newly developed quadrature free approach aims at solving this problem by choosing simple monomial expansions for the basis set, thus making the evaluation of integrals simpler, and the matrices $\mathbf{M}$ and $\mathbf{K}$ sparser. The monomial expansions will be of the form $\xi^i\eta^j$. (For e.g. a second order basis set can be $\mathbf{B} = \{1, \xi, \eta, \xi^2, \xi\eta, \eta^2\}$. However, there are two drawbacks of the quadrature free approach. The first is that the condition number of the mass matrix is very high when monomials are used as basis functions. The second is that the evaluation of boundary integrals in Eqn. (8) will involve edge transformations. Hence, evaluating the boundary integrals in the quadrature free approach will require relatively complex coding and more computational effort. But this increase in computation effort will be offset by the decrease owing to the simplified calculation of the mass and stiffness matrix integrals.

On the other hand, if the flux is *linear*, using either Lagrange polynomials or the monomials, the integrals in $M_{ij}$ and $K_{ij}$ can be calculated analytically and stored before the main computation, without much usage of the memory. The mass matrix computed using Lagrange polynomials will be denser, but with a relatively lesser condi-

tion number compared to the mass matrix computed using monomials. The calculation of the boundary integral will be easier and faster using the Lagrange polynomials.

# 4 Results From the Implementation of the DG Method

Several programs have been written to implement and test the quadrature free DG method in one and two dimensions. The results from these programs for the linear scalar advection equation in one and two dimensions using both the Lagrange polynomials and monomials are presented. A nonlinear advection equation in one dimension is solved using the quadrature free approach. A periodic boundary condition is implemented for both one and two-dimensional calculations. Time marching is accomplished using Crank Nicolson's $2^{nd}$ order scheme, a Fourth–order Runge–Kutta explicit scheme, and the Total Variation Bounded Runge–Kutta three (TVBRK3) stage method.

## 4.1 One dimensional calculations

The test equations are

$$\frac{\partial u}{\partial t} + a\frac{\partial u}{\partial x} = 0 \tag{12}$$

and

$$\frac{\partial u}{\partial t} + a\frac{\partial (u^2/2)}{\partial x} = 0 \tag{13}$$

on the domain $0 \leq x \leq 10$ with periodic boundary conditions.

The solution to the linear problem (12) is obtained with two initial conditions. The first is a half sine wave over a unit interval, and the second is a normal shock. While using the monomials, the initial condition was expanded as a Taylor series about the center of each element. The solution obtained using Lagrange polynomials is shown in figures 2a($1^{st}$ order approximation polynomials with $2^{nd}$ order time marching) and 2b ($2^{nd}$ order approximation polynomials with $4^{th}$ order time marching).

The programs for the implementation of the DG method in one dimension are written in Matlab. The interval from $x = (1, 10)$ is divided into 100 parts: that is, the value of $\Delta x = 0.1$. It is observed that the time step required for stability decreases as the order of spatial approximation increases.

The calculations for the linear advection equation with monomials are shown in Fig. 3a, b and c. It was observed that the use of monomials lead to oscillations in the approximate solution where the exact solution had sharp discontinuities, as can be seen in Fig. 3b. Finally, the solution for the nonlinear Eqn. 13 is shown in Fig 3d. The initial condition was a sine wave, which transformed into an 'N'–wave after sufficient time.

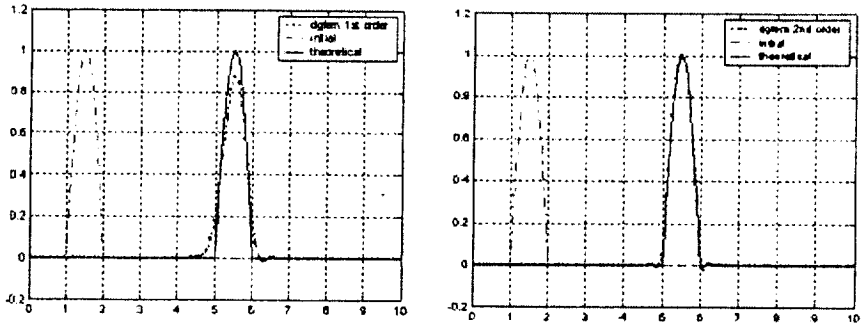

a b

Figure 2: One dimensional calculations using Lagrange polynomials

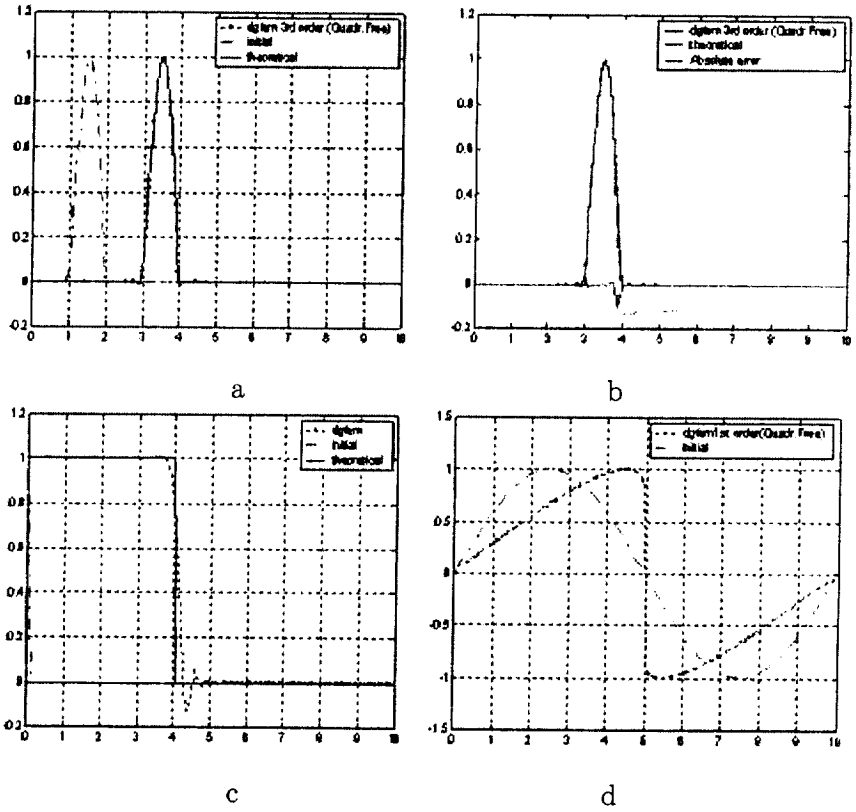

a b

c d

Figure 3: One dimensional calculations using monomials. (a) $3^{rd}$ order approximation monomials with $3^{rd}$ order time marching, (b) Absolute error in the calculation, (c) Calculations with an initial condition of a normal shock wave, (d) Solution for the nonlinear advection equation.

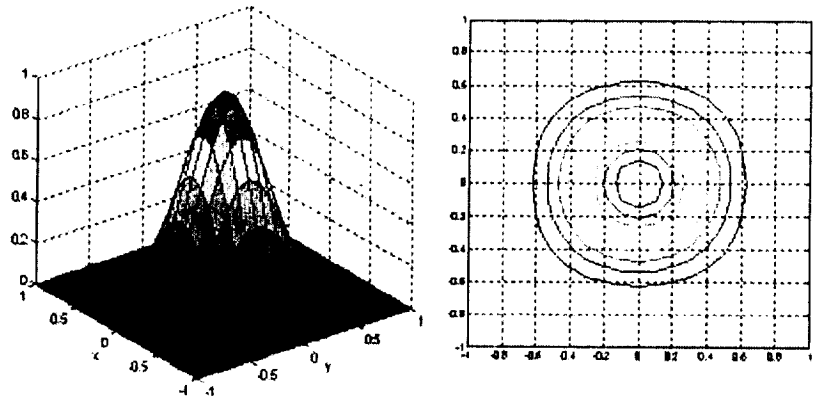

a b

Figure 4: The initial condition. (a) The sine wave pulse with unit maximum value at the center of the domain. (b) a contour map of the initial condition.

## 4.2 Two dimensional calculations

### 4.2.1 The advection equation

The test equation is

$$\frac{\partial u}{\partial t} + a\frac{\partial u}{\partial x} + b\frac{\partial u}{\partial y} = 0 \tag{14}$$

$$u(0, x, y) = [\sin(\pi x)\sin(\pi y)]^4$$

on a periodic square domain $-1 < x, y < 1$ . The grid is made up of 800 similar right angle triangles. The program is written in Fortran 90. The basis set is made up of Lagrange polynomials of up to second order and monomials of up to $4^{th}$ order. The initial condition is shown in Fig. 4.

Figure 5 shows the results for the case with the basis set made up of linear monomials. A similar result is obtained with all other choices of basis functions. The speeds of the wave in the $x$ and $y$ directions are taken to be the same. It is observed that the size of the time step required for a stable solution decreases as the order of approximation is increased.

## 4.3 Calculations for the linearized Euler equations in two dimensions

Consider the propagation of an acoustic pulse in a constant mean flow. The linearized Euler equations are given by,

$$\frac{\partial U}{\partial t} + \frac{\partial E}{\partial x} + \frac{\partial F}{\partial y} = 0 \tag{15}$$

with

$$U = \begin{Bmatrix} \rho \\ u \\ v \\ p \end{Bmatrix}, E = \begin{Bmatrix} M_x\rho + \rho_0 u \\ M_x u + p/\rho_0 \\ M_x v \\ M_x p + \rho_0 u \end{Bmatrix}, F = \begin{Bmatrix} M_y\rho + \rho_0 v \\ M_y u \\ M_y v + p/\rho_0 \\ M_y p + \rho_0 v \end{Bmatrix}$$

where $\rho, u, v, p$ are the flow variables, and $M_x$ and $M_y$ are the values of the mean flow in the $x$ and $y$ directions respectively, non-dimensionalized by the speed of sound based on the mean thermodynamic values, and $\rho_0$ is the mean flow density.

The finite element discretization of the above differential equation results in a system of equations that can be written as,

$$\begin{bmatrix} M & 0 & 0 & 0 \\ 0 & M & 0 & 0 \\ 0 & 0 & M & 0 \\ 0 & 0 & 0 & M \end{bmatrix} \frac{\partial U}{\partial t} + \begin{bmatrix} K_{11} & K_{12} & K_{13} & 0 \\ 0 & K_{22} & 0 & K_{24} \\ 0 & 0 & K_{33} & K_{34} \\ 0 & K_{42} & K_{43} & K_{44} \end{bmatrix} U = \begin{Bmatrix} F_1 \\ F_2 \\ F_3 \\ F_4 \end{Bmatrix} \tag{16}$$

where $M$ and $K_{ij}$ are the mass and stiffness matrices, and $F_1 \ldots F_4$ are the right hand side vectors of the corresponding individual equations.

### 4.3.1 Results

The domain is divided with unstructured triangulation. Basis sets of degree 1 and 2 (order 2 and 3 respectively) are used. A square domain is considered, with a uniform mean flow from the left to right, over a rigid bottom wall. An initial Gaussian distributed acoustic pulse is located near the lower boundary, as shown in Fig 6.

Reflective boundary conditions are imposed on the lower boundary, and non-reflecting boundary conditions are imposed on the three other boundaries. The radiating boundary conditions are implemented using characteristic variables [5]. Figures 7a and b show the computed propagation of the acoustic disturbance with the mean flow. Some reflections are observed near the right boundary, and these are due to the characteristic method of boundary condition used, as mentioned in [5].

# 5 Conclusions and Future Work

The linear advection equation with periodic boundary conditions has been solved using the DG method in one and two dimensions. A qualitative comparison of the Lagrange polynomials and simple monomials as choices for the basis set has been made. A basis set comprised of simple monomials is more suited for h-p refinement of the solution. The choice of monomials for nonlinear convective equations is thought to be advantageous compared to the Lagrange polynomials under the formulation described, in which, the nonlinear flux is evaluated by multiplying or dividing the approximating expressions for the basic variables. However, the formulation involving the nonlinear flux could also be solved using iterative techniques. It remains to be investigated